Journal of Applied Physics TUTORIAL scitation.org/journal/jap

Photoacoustic and photothermal and the photovoltaic efficiency of solar cells: A tutorial

Cite as: J. Appl. Phys. **131**, 141101 (2022); doi: 10.1063/5.0088211
Submitted: 14 February 2022 · Accepted: 11 March 2022 ·
Published Online: 8 April 2022

A. C. Bento,[1] N. Cella,[2] S. M. Lima,[3] L. A. O. Nunes,[4] L. H. C. Andrade,[3] J. R. Silva,[3] V. S. Zanuto,[1] N. G. C. Astrath,[1] T. Catunda,[4] A. N. Medina,[1] J. H. Rohling,[1] R. F. Muniz,[5] J. W. Berrar,[1] L. C. Malacarne,[1] W. R. Weinand,[1] F. Sato,[1] M. P. Belancon,[6] G. J. Schiavon,[7] J. Shen,[8] L. C. M. Miranda,[9] H. Vargas,[10] and M. L. Baesso[1,a)]

AFFILIATIONS

[1]Departamento de Física, Universidade Estadual de Maringá, 5790, Maringá 87020-900, PR, Brazil
[2]Instituto Politécnico, IPRJ, Universidade do Estado do Rio de Janeiro, UERJ, P.O. Box 97282, Nova Friburgo 28601-970, RJ, Brazil
[3]Centro de Estudos em Recursos Naturais—CERNA, Universidade Estadual de Mato Grosso do Sul-UEMS, Dourados 79823-351, MS, Brazil
[4]Instituto de Física de São Carlos, Universidade de São Paulo, 369, São Carlos 13560-970, SP, Brazil
[5]Departamento de Ciências, Universidade Estadual de Maringá, Goioerê 87360-000, PR, Brazil
[6]Departamento de Física, Universidade Tecnológica Federal do Paraná, Pato Branco 85503-390, PR, Brazil
[7]Departamento Acadêmico de Eletrônica, Universidade Tecnológica Federal do Paraná, Via Rosalina Maria dos Santos, 1233, Campo Mourão 87301-899, PR, Brazil
[8]National Research Council Canada, Energy, Mining and Environment Research Centre, 4250 Wesbrook Mall, Vancouver, British Columbia V6 T 1W5, Canada
[9]Instituto Nacional de Pesquisas Espaciais, São José dos Campos, SP, Brazil
[10]Centro de Ciência e Tecnologia, Laboratório de Ciências Físicas, Universidade Estadual do Norte Fluminense, Av. Alberto Lamego 2000, Campos dos Goytacazes, RJ 28015-620, Brazil

Note: This paper is part of the Special Topic on Non-Invasive and Non-Destructive Methods and Applications Part I â Festschrift.
[a)]**Author to whom correspondence should be addressed:** mlbaesso@uem.br

ABSTRACT

Optical losses are the major drawback to overcome in the solar energy industry and development. Conversion of solar radiation into heat accounts for over 80% of the incident solar energy, which is driven by several aspects like the chosen design and encapsulation of the devices, built-in materials, and the mismatch between the solar spectrum and the active cell's bandgap energy. Photoacoustic (PA) and photothermal (PT) methods are characterization techniques based on the heat generation after the illumination of a material and respective detection. Since the beginning of the solar panel industrial development, these methods have been successfully applied to evaluate the photovoltaic efficiency of devices and the thermophysical parameters of related materials. Here, we present the state-of-art of application of these PA and PT methods to characterize solar cell devices and their built-in materials. Historical aspects, conceptual mechanisms of the basic phenomena, and perspectives on their application for energy-conversion measurements in the new frontier of solar cell research will be discussed.

I. INTRODUCTION

The photovoltaic effect was discovered by Edmond Becquerel in the year 1839. He observed electrical effects produced by the influence of the sun rays illuminating the chemical reactions that took place when two liquids come into contact.[1] As he used two platinum electrodes, one in each of these liquids, and these two electrodes themselves experienced the effects of radiation, he ran out another experiment to observe electrical effects produced by the influence of the sun rays illuming, in a non-uniform way, two platinum electrodes in an electrochemical cell.[2] In this second experiment, he was careful to avoid the electric current produced by the difference of temperature between these two electrodes, as a consequence of the non-uniform illumination, i.e., avoiding thermoelectricity produced by the caloric component of the sun rays.[3] In that time, the sun rays were assumed to be composed of three kinds of radiation: chemical, visible, and heating.[4]

During many decades, E. Becquerel and a great number of investigators have been studying the photovoltaic effect using different materials for the electrolytes and for the electrodes, as well as using the "dry" or "wet" cell types.[5] Among the numerous works, some of them were considered as a milestone for this research area, such as the discovery of the selenium's photoconductivity in 1873[6,7] and the photoelectric effect in 1887.[8] Between 1875 and 1878, a better understanding about the action of the sun rays on selenium was achieved.[9,10] After that, in 1880, Alexander Graham Bell invented and made improvements on the selenium cells,[11] shown in Fig. 1, and applied this selenium cell in his new invention, the photophone, still in the year 1880,[12] shown in Fig. 2.

During the experiments with the photophone, still in 1880, A. G. Bell discovered the "photophonic phenomena" (nowadays "photoacoustic effect"). It was discovered when he focused the sun rays, modulated at audible frequency, on a rubber diaphragm of a hearing tube, as shown in Fig. 3, taking off the photophone apparatus: the speaker, the selenium cell, the battery, and the telephone receiver.[12] In 1881, more experiments were carried out by A. G. Bell to better understand this new phenomena (photophonic phenomena) and details can be found elsewhere.[13]

Also, with the continuum progress in producing a "dry" selenium cell, the first practical solar cell, based on the photoconductivity of selenium, was made in 1883.[14]

In 1888, the photoelectric effect was observed and studied on electrostatically charged bodies[15] and the first solar cell based on the photoelectric effect was made.[16] Still in 1888, using the already well-known thermopile,[17] the first solar cell based on the thermopile was made.[18] However, the conversion efficiency of all these kinds of solar cells was very low and no practical/commercial use was developed. The photoelectric effect was finally explained by A. Einstein in 1905.[19] Almost half-century was necessary for the first silicon solar cell to be invented in the Bell's Laboratory,[20] as shown in Fig. 4. Finally, in 1954, a milestone event was the invention of the first single crystal silicon solar cell with 6% photovoltaic efficiency, at Bell Labs.[21] This invention was patented in 1957.[22] Since that time, a p-n junction was the basis of the development of "dry" solar cells. On the other hand, the development of "wet" solar cells had a continuous improvement until the end of the 1970 decade.[23–29]

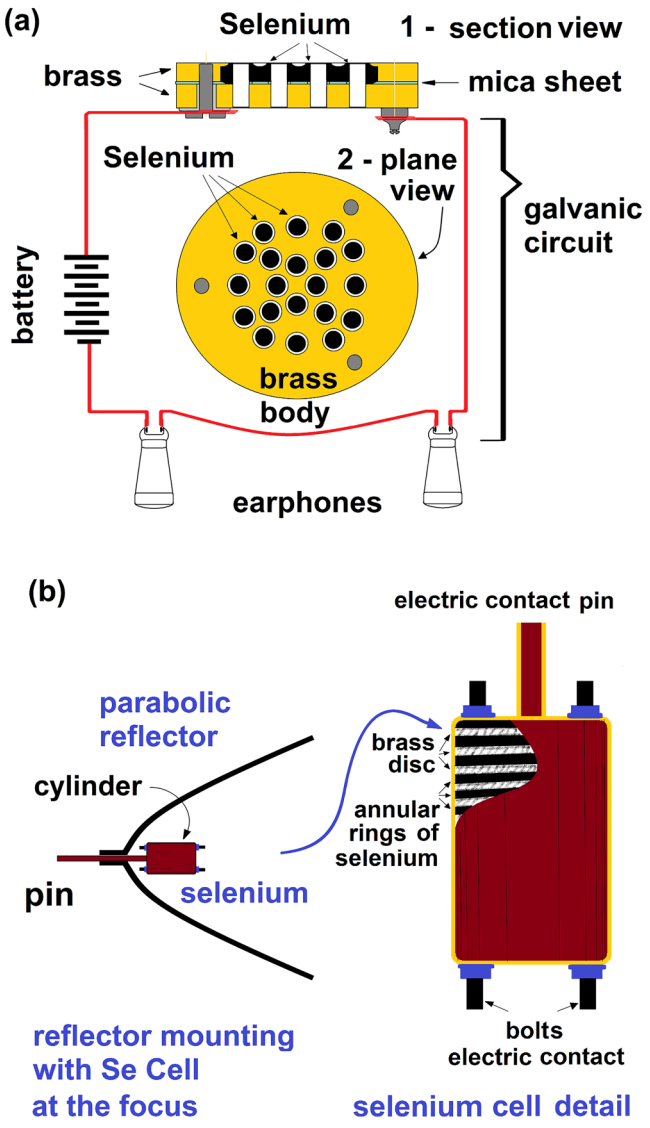

FIG. 1. Two types of selenium cells: (a) a disk form to be used at the lens focus and (b) a cylinder form to be used in a parabolic reflector mirror with the selenium cell at its focus. Adapted from Refs. 11 and 12.

Nowadays, solar cells are given a considerable environmental, economic, and scientific attention toward gaining large scale of worldwide energy production.[30–51] The technological advances in the last decades resulted in silicon-based solar panels with a working life of about three to four decades and the new emerging technologies the so-called "third generation solar cells' based on tandem, perovskite, dye-sensitized, organic, as well as spectral converters.[30] The photovoltaic efficiency is a paramount parameter attracting the attention of many researchers in the scientific community. For example, for silicon-based commercial panels, a

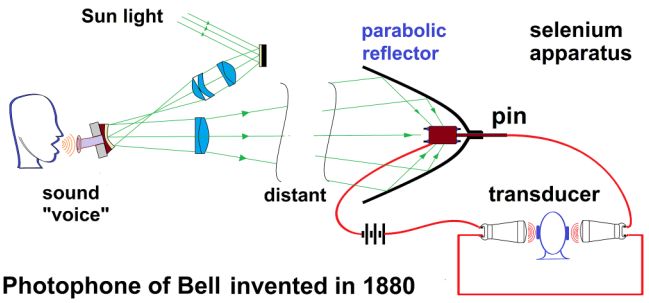

FIG. 2. The photophone invented by A. G. Bell in 1880. Sun rays are reflected in the mirror diaphragm, vibrating with the voice of a speaker, and being received by the selenium cell apparatus. The electrical oscillating signal from the selenium cell is detected by a circuit with a battery and telephone receiver. Adapted from Ref. 12.

significant part of the incident sunlight energy is converted into heat due to the mismatch between the silicon bandgap and the sunlight spectrum, as illustrated in Fig. 5(a), accounting for a nowadays losses over 80% of the incident solar energy.[30] In this scenario, from the scientific and technological point of view, the photoacoustic (PA) and photothermal (PT) methods are of great importance to evaluate the solar cell energy-conversion processes since these methods are based on the detection of the induced heat in a sample as a consequence of their lighting excitation. Therefore, these methods are paramount in the evaluation of the photovoltaic efficiencies of the devices and the thermophysical parameters of related materials. Here, we present the state-of-art of application of these PA and PT methods to characterize solar cell devices and their built-in materials. Historical aspects, conceptual mechanisms of the basic phenomena, and perspectives on their applications for energy-conversion measurements in the new frontier of solar cell energy research will be discussed.

For the sake of organization and historical aspects, first, in this tutorial we focus on the PA and PT study on the initial photovoltaic

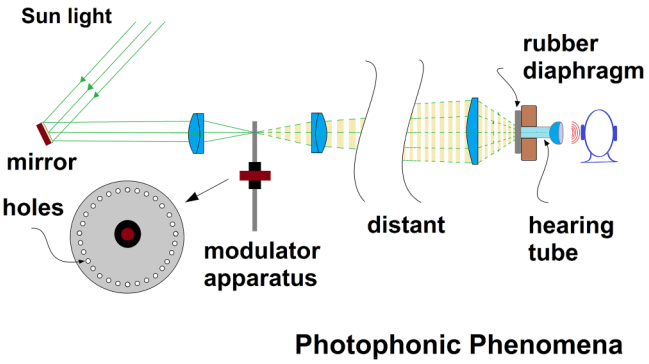

FIG. 3. The "photophonic phenomena." The sun rays are interrupted by an apparatus that modulates these rays at audible frequencies. Focusing this modulated sunlight on the surface of the rubber diaphragm of a hearing tube, a sound was heard. Adapted from Ref. 12.

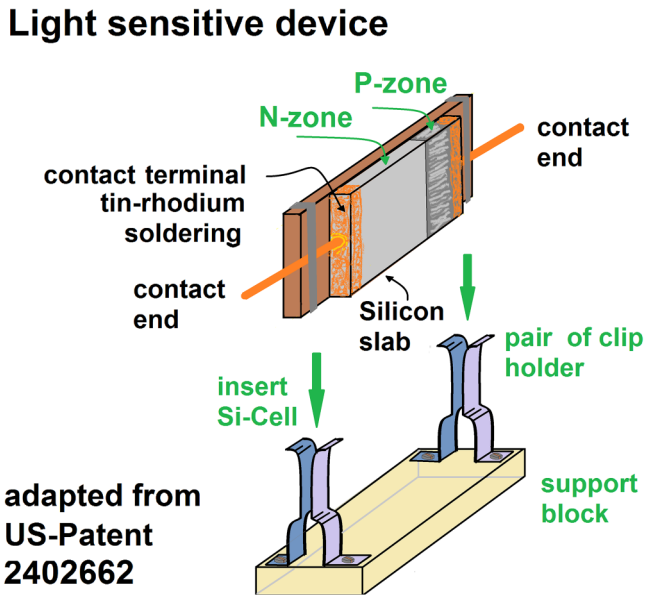

FIG. 4. The first silicon solar cell invented by Russel Shoemaker Ohl.[20]

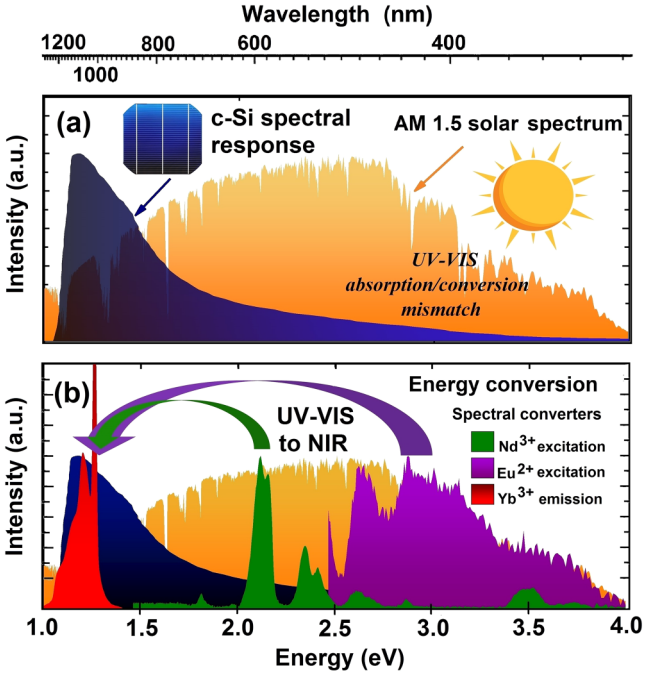

FIG. 5. (a) Orange background is the solar spectrum (AM1.5G) in the UV-Vis-NIR regions. The gray is the spectral response of the c-Si. The spectral mismatch is quite evident. (b) Purple and green curves are the optical absorption coefficients of Eu^{2+} and Nd^{3+} activators, and the red curve is the Yb^{3+} sensitizer emission around 980 nm, close to the c-Si bandgap.

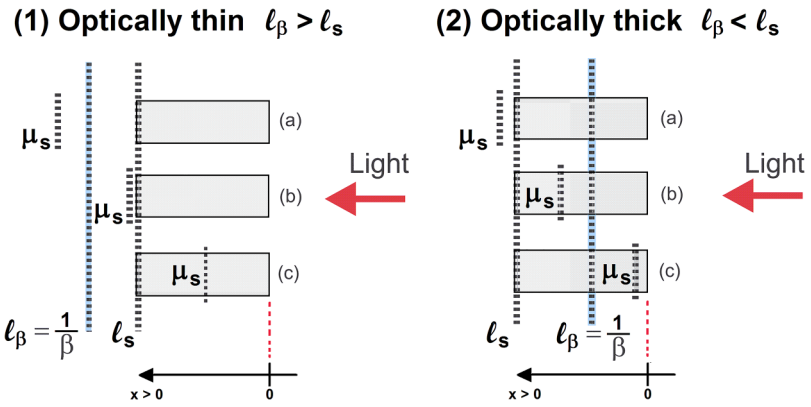

FIG. 6. Optically thin and thick regimes depending on the thermal diffusion length (μ_s), the light penetration depth (ℓ_β), and the sample thickness (ℓ_s).

devices. After that, the methods are discussed in terms of the energy-conversion measurement in the new generation of solar cell materials such as those containing sensitizer-activator ions dedicated to convert ultraviolet and visible lights into the near-infrared, illustrated in Fig. 5(b), known as spectral converters.[30,31,36,42,47–50]

II. PHOTOACOUSTIC SPECTROSCOPY (PAS)

The photoacoustic spectroscopy (PAS) technique[52–56] was used, for the first time, for the determination of photovoltaic energy-conversion efficiency in a-Si solar cell, in the end of 1970 decade.[57] After that, in the next two decades, many works based on photoacoustic and/or photothermal techniques have been applied for the analysis of power loss mechanisms in solar cells;[58–60] the characterization of photovoltaic cells;[61,62] the energy balance analysis of photovoltaic cells;[63] the study/understanding the photoacoustic signal in solar cells;[64–68] among other works. In this way, photoacoustic and photothermal methods were successfully developed as photocalorimetric techniques for the characterization of photovoltaic devices. In the last two decades, many parameters were obtained/monitored using the photoacoustic technique, such as: the optical absorption spectrum; [69–73] optical absorbance;[72] the bandgap energy;[71,73] the interface recombination velocities;[74] carrier recombination time and thermal diffusivity,[75] among other parameters considered in the development of solar cells.

One particular characteristic of the PAS is that the effective thickness of the sample that contributes to the photoacoustic signal is defined by the thermal diffusion length (μ_s), the light penetration depth ($\ell_\beta = 1/\beta$), in which β is the optical absorption coefficient, as shown in Fig. 6. The evaluation of these parameters allows the use of the technique to perform depth profile analysis and energy transfer processes in a sample. In the case of semiconductors, bulk and surface absorption, below and above the bandgap, respectively, can be decoupled with this method. This feasibility of the methods is of great importance to study layered samples to access each layer property and the relation to the device performance.

A. PAS pioneering characterization of a photovoltaic Si solar cell after Cahen (1978)

The first photoacoustic characterization of photovoltaic devices was done by Cahen in 1978.[57] He used a commercial silicon solar cell as a sample. Applying the resistance load over the Si photovoltaic cell, the power output (a more recent current–voltage characteristic curve for Si solar cell can be found elsewhere[76]) and the relative photoacoustic signal were monitored. The results are shown in Fig. 7(a). In the theoretical model used, for the photoacoustic determination of photovoltaic energy-conversion efficiency, was assumed that only photovoltaic process took place and, for a specific resistance load L, the photoacoustic signal, $S(L)$, was given by[57]

$$S(L) = \beta_{frac}[1 - \gamma(L)], \tag{1}$$

in which β_{frac} is the fraction of light absorbed by the sample in the photoacoustic cell (PA cell) and $\gamma(L)$ is the energy-conversion efficiency for the photovoltaic process, for a specific resistance load R_L. Therefore, more is the photovoltaic efficiency (or power output) less is the heat generated by nonradiative de-excitation and less is the detected photoacoustic signal. This can be observed in Fig. 7(a), where the optimal load obtained was $R_L = 5.1\ \Omega$. The photovoltaic conversion efficiency is zero for the extremely high resistance load [open circuit, "oc," $\gamma(\mathrm{oc}) = 0$] and, from Eq. (1), the photoacoustic signal for the open-circuit condition is equal to the fraction of light absorbed by the Si Solar cell in the PA cell, $S(oc) = \beta_{frac}$. Thus, the energy-conversion efficiency is given by[57]

$$\gamma(L) = \left[\frac{1}{S(oc)}\right][S(oc) - S(L)]. \tag{2}$$

A remark should be made here about the convenient way that $\gamma(L)$ has been measured. The photoacoustic signals $S(oc)$ and $S(L)$ were measured under identical illumination conditions, because the sample is not taken out of the PA cell. In the designed PA cell, used in this work, Fig. 7(b), the sample constitutes the backing wall (i.e., the wall opposite to the frontal optical window). Details of this kind of photoacoustic cell have been presented elsewhere.[77] The values obtained for the photoacoustic signals were for the open-circuit $S(oc) = 54$ units and for the optimal load resistance $S(5.1) = 44.5$ units. Using these values in Eq. (2), $\gamma(5.1) = 0.175$, i.e., 17.5% of energy-conversion efficiency for the illumination conditions used (IR and near-UV filtered incident Xe light), with

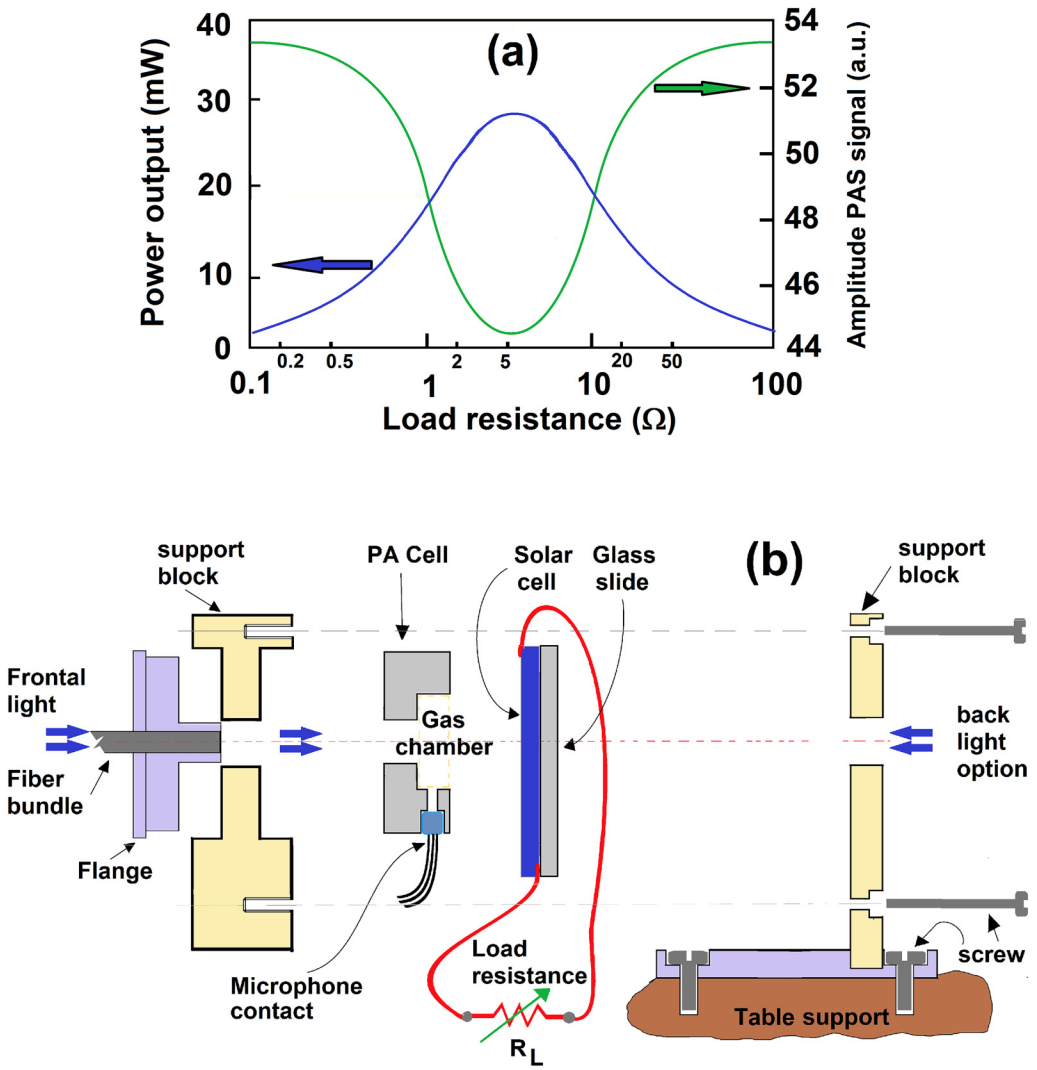

FIG. 7. (a) Amplitude of the photoacoustic signal and electrical output power as a function of resistance load over the silicon photovoltaic cell. The modulation frequency used was 540 Hz. Details of the experimental condition can be found elsewhere;[57] (b) the cut view of the PA cell used in this experiment. Adapted from Refs. 57, 59, and 77.

incident intensity on the PA cell of 160 mW cm^2.[57] This work illustrates the application of photoacoustic spectroscopy to characterize photovoltaic devices. After that, Cahen and collaborators point out that: (1) the PA signal is a result of two contributions, i.e., (i) the heat generated by the recombination of photogenerated carriers and (ii) the heat generated by the recombination of injected carriers;[64] (2) there are changes in the maximum I-V characteristics (power output) and in the minimum amplitude of the PA signal curves when the Si solar cell is potentiostatically loaded or resistance loaded;[59] (3) the mechanism of power loss (or power dissipation) in the Si solar cell can be separated by the relation between the illuminated area (inside or outside of PA cell) and the detected area of the PA cell, in PA signal as a function of applied photovoltage (or load resistance) on solar cell;[59,78,79] and (4) the mechanism of power loss (or power dissipation) in the Si solar cell can be separated by the variation of the distance between the illuminated area (outside of PA cell) and the detection area (area of PA cell) at a fixed modulation frequency or for a fixed distance and variation of the modulation frequency, due to the lateral direction effects of the thermal diffusion and the electronic carrier diffusion.[68]

The most traditional experimental setup used nowadays for the PAS is illustrated in Fig. 8. It contains a Xe lamp for modulated excitation intended to do spectroscopic measurements, having a monochromator, a mechanical chopper, optics for alignment and removal of superior order of diffractions, a microphone and the data acquisition electronic and software. The additional non-

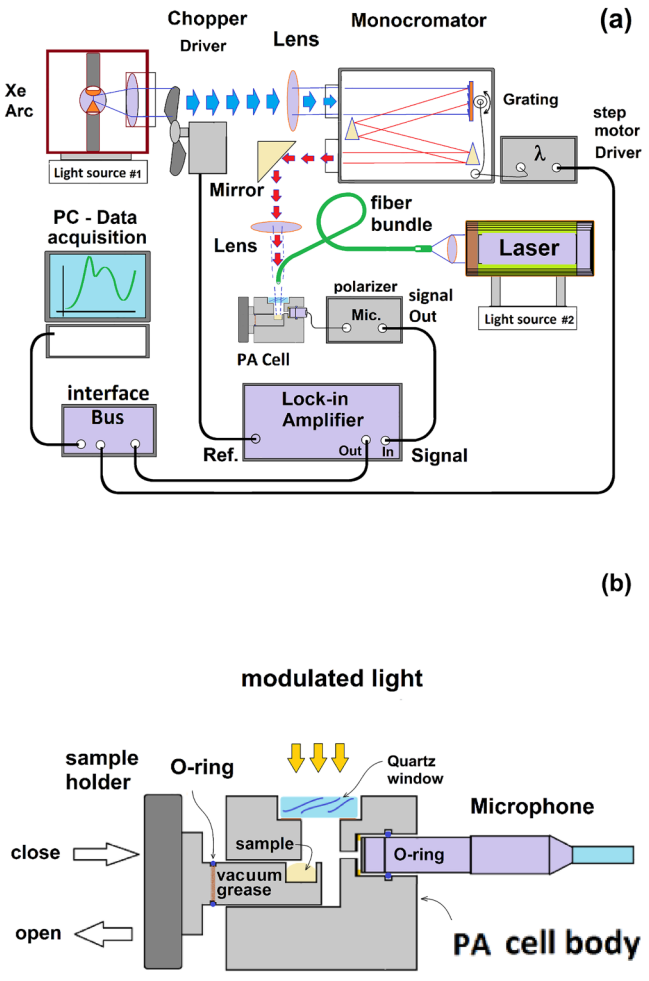

FIG. 8. (a) Photoacoustic spectroscopy experimental setup and (b) detail of the photoacoustic cell.

modulated excitation light, usually lasers or LEDs, can be used for several applications of photophysics and energy-conversion processes,[80] as will be used later on.

III. PHENOMENOLOGICAL ASPECTS OF THE PA AND PT TECHNIQUES

Photothermal techniques include a broad spectrum of methods. In general, the thermal wave (TW) vs carrier density waves (CDWs) concept is the principal issue to be considered to understand the heat transport phenomena in electronics materials, especially for solar cells, in which the knowledge of the nature of the light conversion in excitation phenomena or carrier generation and the consequent diffusion of carriers is an essential issue. The standard thermal wave methodology, which is the base for the majority of PA and PT techniques using a source of modulated light, could address a part of this problem, dealing with modulated electric fields in an electronic medium, but many other phenomena may occur in the bulk or surface and play important roles in the efficiency of converting light to electric current, especially in the solar cells intended to be discussed here. This subject was recently discussed in a condensed way by Mandelis, emphasizing the derivations of the diffusion-wave fields in an easy-to-follow manner. He introduced some new mathematical concepts about the so-called carrier-density fields as a contributing wing allied to the thermal wave field for electronics materials when impinged by modulated light.[81]

The concept of diffusion-wave fields (DWFs) was proposed as a new understanding of the photothermal generation of free carriers, with a suitable mathematical formalism to solve analytically the problems connecting experiments of characterization for electronic devices using these methods. It stands that the DWF must take into account all electronic properties allied to the heat transfer in the medium, specifically to treat the electronic carriers using the concept of carrier-density field or carrier-diffusion field (CDW), which essentially differs from the traditional thermal-wave field (TWF). It treats a diffusion current of particles (electrons and holes) rather than considers it as continuous dissipative energy. The DWF was considered as taking place under modulated excitation of the free carriers. Combining both DWF with TWF under the same modulated source, the "thermo-electronic effect" arises and should be considered in any problem of electronic transport involving characterization of electronic materials, demanding, therefore, the definition for a new wavenumber, conceptually proposed as

$$\sigma_e = [(1 + \omega\tau)/D^*)\tau], \tag{3}$$

defined as dependent on the modulation of light (ω), the average lifetime of carrier's recombination (τ) and diffusivity of carriers (D^*) in the electronic diffusion length $[L_e = ((D^*)\cdot\tau]^{1/2})$, while for the conventional diffusion in the TW, the wavenumber is defined as

$$\sigma_d = [(i\omega\tau)/\alpha]^{1/2}, \tag{4}$$

with α being the semiconductor thermal diffusivity.

Invoking the early experiments on solar cell characterization, one can see that the statement of Mandelis[81] on the new wavenumber concept was already there but not yet understood or fully explained. After Cahen's[57] work applying PA cells for photovoltaic efficiency characterization of a-Si solar cells, Nordal/Kanstad used the radiometry method (PTR) in 1985[82] and following them, Faria *et al.* used the pyroelectric method (PPE) in 1986[65] and both of them called attention over the necessary precaution on doing absolute measurements of photovoltaic conversion efficiency using photothermal methods. It was further demonstrated that the photoacoustic method proposed by Cahen is only applicable if effects as luminescence, Joule heating of carriers and photochemistry processes, among others could be neglected. Using the photopyroelectric method (PPE) compared to photoacoustic (PA), Mello *et al.*[61] pointed out that PPE senses the Joule effect in a "heat sink" style, while the PA senses only the contribution that reaches the frontal surface of the solar cell, being the diffusing heat toward the

back interface or to the borders and then completely dissipated. Further, Riette *et al.*[62] using the non-contact method of photothermal beam deflection (PTD) better described such dissipation effects, and concluded that both internal losses are not sensed by the PA method and PTD can provide both the optimal internal load resistance and conversion efficiency.

These experiments since performed in a relative low modulation frequency (fewer hundred Hz) are compatible with heat dissipation characterization in electronics materials, which is not true for much higher modulation frequencies (several dozen kHz) conditions in which contribution from carriers' recombination effect and carriers' diffusion are most likely to be present. In this case, CDW and TW concepts should be considered in the analysis of any photothermal experiment that aims to characterize solar cells using a high modulation frequency.

IV. BANDGAP DETERMINATION BY PAS

Photoacoustic spectroscopy has been extensively used in the characterization of optical properties of semiconductors.[54,83–87] The mechanisms responsible for the generation of the photoacoustic signal depend directly on the energy used in the measurements and are particularly distinct when the photon energy is above or below the bandgap energy (E_g).[54,83–90] If the absorbed energy ($h\nu$) is higher than E_g, an excess of photo-injected carriers with energy $h\nu - E_g$ in the conduction band is created and information regarding the carrier transport properties can be assessed. Followed by de-excitation due to electron–phonon collision, this process releases the excess of energy to the lattice, diffusing through the sample. This chain of events eventually restores equilibrium by recombination with the holes in the valence band.

PAS has been used for *in situ* measurements of surface properties of metal electrodes,[91] semiconductor electrode reaction,[92] and quantum and energy efficiencies of the surface of a semiconductor.[93] Mandelis *et al.* have continuously contributed to the photothermal spectroscopy characterization of semiconductors over the past decades. Photothermal deflection and photoacoustic detections have been used for monitoring internal quantum and energy efficiencies and nonradiative energy-conversion channels in semiconductor photoelectrochemical cells.[94–96] An all-optical deep-level photothermal spectroscopy was used for detecting the effects induced by thermal transport to and from the band edges and for the characterization of deep-level generating defects in semiconductors.[97–99] Frequency-domain photoluminescence, and lock-in thermographic imaging and infrared frequency-domain photocarrier radiometry were used to characterize a variety of silicon-based solar cells[100–105] and to study charge carrier recombination processes and sub-bandgap energy states in colloidal quantum dots thin films.[106–108]

The bandgap energy of semiconductors is a key parameter for the electronic and optoelectronic areas[60,89,90,109–111] and its value can be obtained using different qualitative approaches. The direct bandgap energy is usually obtained from the absorption edge of a linear fitting in the plot of the square of the absorption coefficient vs the photon energy.[112] For indirect bandgap determination, the plot of the square root of the product between the absorption coefficient and the phonon energy vs the photon energy[113] is used. However, sample preparation conditions, purity of the raw materials and surface optical finishing interfere in the determination of the absolute value of the optical absorption coefficient in the region where the bandgap occurs.[83,113] Several optical methodologies have been used to detect optical absorption spectra, including PAS and photoreflectance spectroscopies.[88–90,114] Conventional PAS is limited when the nonradiative recombination in the band edge is minimized, while with the photoreflectance techniques usually the fluorescence cannot be separated from the probe light.

By exciting the sample with continuous laser energy above and below the bandgap, PAS has also been used to determine the energy of the bandgap directly from the experimental optical absorption spectra of a bulk single crystal PbI_2 and of a thin film 4H-SiC crystal.[73] The experimental setup used was a photoacoustic spectrometer with the samples placed in a conventional photoacoustic cell,[115] as schematically illustrated in Fig. 8. The light source was obtained from a 1000 W Xe lamp and was modulated at a frequency of 20 Hz. In the original work,[73] an Ar^+ ion laser tuned at 457 and 514.5 nm was used as a continuous light source, while a He–Ne laser was used at 632.8 nm. The photoacoustic spectra were recorded while the samples were excited only by the modulated light and by modulated light under continuous light excitation at a fixed wavelength. The signal variation with and without continuous excitation was also investigated by maintaining the wavelengths of the modulated and continuous light sources fixed and collecting the photoacoustic signal as a function of time, by turning the continuous light on and off. The same effects observed in the spectra were measured in the time response regime of the photoacoustic signal when the modulated and continuous wavelengths are maintained fixed.

Figure 9 shows the photoacoustic spectra of lead iodide (PbI_2) with or without excitation by continuous laser light as a function of photon energy, obtained from Ref. 73.

The spectrum of the non-irradiated sample with laser shows an onset of the optical absorption band around 2.3 eV. By assuming the bandgap value as the photon energy at the absorption edge, $E_g = (2.35 \pm 0.05)$ eV can be identified as the fundamental bandgap energy. However, if the optical bandgap is evaluated from the plot of the square of the absorption coefficient *vs* the photon energy,[116] $E_g = (2.28 \pm 0.01)$ eV. In this manner, the correct value of the bandgap energy is difficult to be established due to the uncertainties in the determination of the absolute value of the optical absorption coefficient in the bandgap edge. Thus, by excitation with continuous light, as shown in Fig. 9, the generated photoacoustic signal varies for energies higher and lower than E_g, but they can be considered the same in the region where the non-irradiated and irradiated continuous light spectra crosses. The crossing of the spectra can be assumed as the value of the bandgap energy, i.e., $E_g = (2.33 \pm 0.01)$ eV.

The decreasing/increasing the photoacoustic signal under continuous light excitation was demonstrated by monitoring the PAS signal as a function of time at fixed modulated and continuous excitations. The same effects observed in the spectra were observed in the time response regime of the photoacoustic signal. The increase of the signal occurs when the modulated light is fixed at 1.96 eV (632.8 nm) and the continuous light fixed at 2.72 eV (457 nm). The time dependent signal is qualitatively described in Fig. 10(a) (bottom). During the time the continuous excitation is off, when only the modulated light (632.8 nm) is incident on the

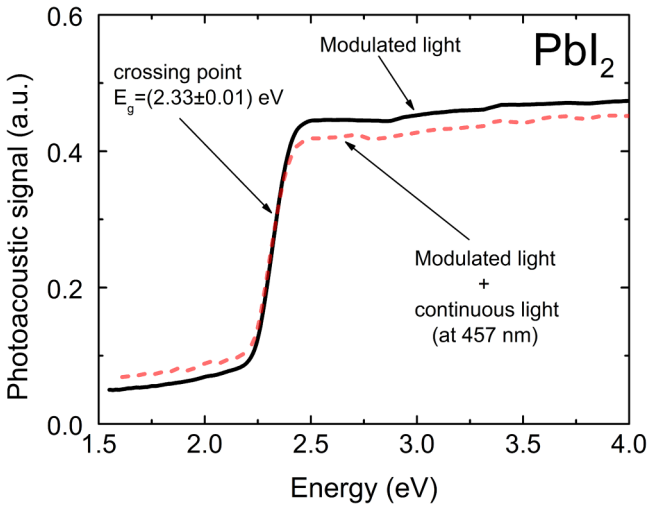

FIG. 9. Photoacoustic signal of PbI_2 as a function of photon energy, obtained from Ref. 73. The crossing of the spectra with and without continuous excitation determines the bandgap energy $E_g = 2.33$ eV. Continuous line shows the signal of the non-irradiated sample, and the dashed line shows the signal obtained for the sample irradiated at 2.72 eV (457 nm, 40 mW).

sample, the photoacoustic signal is low since the absorbed energy is not sufficient for the electrons to reach the conduction band.

Under continuous excitation, the photoacoustic signal increases and may be explained as follows. When continuous light with energy higher than the bandgap is incident, the excited electrons are promoted to the conduction band. Then, the continuous-light-induced free carriers absorb the modulated light resulting in an intraband transition. As a consequence of the higher probability of the modulated light to be absorbed by the excess of free carriers, a higher photoacoustic signal is generated. This mechanism may dominate the signal generation. The proposed simplified model to explain the thermal generation channel of the PAS signal under continuous excitation is illustrated in Fig. 10(a).

The decrease of the photoacoustic signal occurs when the modulated light is fixed at 2.41 eV (514.5 nm) and the continuous light at 2.72 eV, shown schematically in Fig. 10(b). With the continuous light off, the modulated light is sufficient for exciting the electrons to the conduction band and from there they decay non-radiatively to the valence band generating the photoacoustic signal. When the continuous light is incident, some conduction electrons (free carriers) may absorb energy at the conduction band inducing an intraband transition. The thermal generating channel in this situation is proposed in Fig. 10(b). In this process, there is an increase in the nonradiative relaxation time and since the photoacoustic signal is inversely proportional to the time of the recombination processes, the generated signal decreases. As the continuous light is off, the photoacoustic signal recovers its original value in both cases.

This experiment is simple to perform, widening the number of available methods for the study of the energy transfer processes and bandgap determination in semiconductors and solar cells.

A. Measurement of thin film thickness by PAS

The thin film thickness in the nanoscale regime is an important parameter toward understanding the functionality of many devices. There are several methods to make the measurements, like x-ray diffractometry, ellipsometry, and spectrophotometry. However, these techniques sometimes are of high cost and present limitations. Photoacoustic spectroscopy was recently developed for thin film thickness measurements considering the condition in which the photoacoustic spectrum provides a pattern of interference fringes as a result of light multireflection in the air/film and film/substrate surfaces,[117] as illustrated in Fig. 11.

Adding both waves, the interference effects result in an intensity of the reflected light given by[117,118]

$$I_R = I_{R1} + I_{R2} + 2\sqrt{I_{R1} I_{R2}}\cos\delta, \tag{5}$$

in which $I_{R1} = R_1 I_0$ and $I_{R2} = R_2(1 - R_1)I_0$ are the intensities of the reflected light at the interface air/film and film/Substrate, respectively. R_1 and R_2 represent the reflection coefficients on the interfaces and δ is the phase difference between the reflected waves,

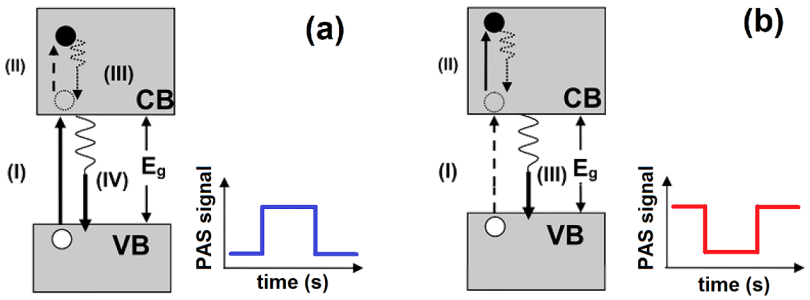

FIG. 10. Simplified model for the thermal generation channel of the PAS signal under the excitation of continuous and modulated light. (a) Probe light modulated at 632 nm (with an energy lower than the bandgap): I—continuous light with energy higher than the bandgap at 457 nm impinges the sample and promotes the electrons to the conduction band. II—intraband transitions occur as the modulated light is absorbed by the free carriers. III–IV—as a consequence, the fast decay induces greater thermal effect, resulting in higher PS. (b) modulated light with energy higher than the bandgap: I—light modulated at 514.5 nm promotes the electrons to the conduction band, II—the continuous light is absorbed in the conduction band, increasing the nonradiative relaxation time, reducing the PAS signal (route III).

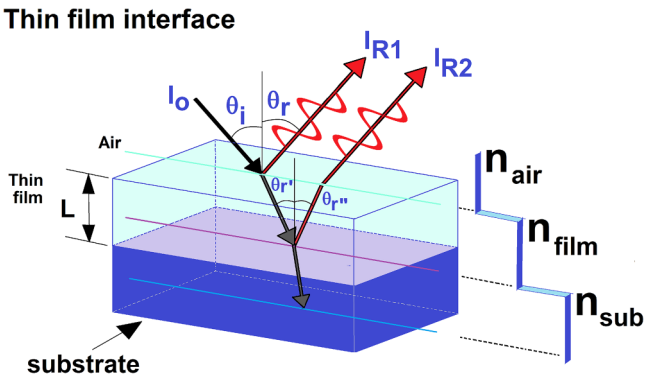

FIG. 11. Multireflection waves in a thin film deposited over a substrate.

given by

$$\delta = \frac{4\pi}{\lambda} n_f \, L\cos\theta_r. \tag{6}$$

Here, $\theta_{r'}$ is the refraction angle of the incident ray, L is the film thickness and n_f is the film refractive index at the wavelength λ.

The refractive index values for the film as a function of λ can be measured using the interferometric technique[119,120] and can be given by Cauchy's equation as

$$n_f(\lambda) = n_0 + \frac{C_2}{\lambda^2} + \frac{C_4}{\lambda^4}. \tag{7}$$

Considering normal incident light ($\theta_r = 0$) and non-absorbent film (transparent), the reflection coefficients and the phase difference can be written as[121]

$$R_1 = \left(\frac{n_f - 1}{n_f + 1}\right)^2, \tag{8a}$$

$$R_2 = \frac{(n_f - n_S)^2 + k_S^2}{(n_f + n_S)^2 + k_S^2}, \tag{8b}$$

$$\delta = \frac{4\pi}{\lambda} n_f L, \tag{8c}$$

in which n_S and k_S are the refraction index and the extinction coefficient of the substrate, respectively.

As a result, the light intensity at the substrate surface (I_S) is obtained by subtracting the reflected intensity (I_R) from the incident one (I_0). Thus, since the photoacoustic signal is proportional to the light intensity that reaches the film surface, it is given by

$$S_{PAS} = S_0\left[1 - \left(R_1 + R_2(1 - R_1) + 2\sqrt{R_1 R_2}\cos\delta\right)\right], \tag{9}$$

in which S_o is the photoacoustic signal measured for the substrate without the film, while R_1, R_2, and δ are given by Eq. (8). Therefore, by performing curve fitting to the experimental photoacoustic spectrum, using Eq. (9), the thin film thickness L value can be obtained, which is the unique adjustable parameter.

Figure 12 shows an example of this measurement performed in a glass thin film deposited in the c-Si substrate.[117] The open and solid black circles are the PAS spectra from the substrate and the sample with the thin film, respectively. The red line is the simulation obtained using Eq. (9). The theoretical model fits the experimental fringes providing in this case a thickness of 620 nm. This range of thickness is difficult to be measured by x-ray diffraction measurements, confirming that the PAS method is complementary to other techniques.

V. PT METHODS FOR DOWNCONVERSION INTERPRETATION IN THE SOLAR CELLS WITH SPECTRAL CONVERTERS

It has been reported that UV-Vis to near-infrared downconversion (DC) in luminescent materials, notably those co-doped with rare-earth (RE) ions, can contribute to improving the efficiency of conversion of light to electricity in Si solar cells.[51] Depending on the used RE ions, a cooperative energy transfer (CET) mechanism can be possible, which converts the not useful UV-Vis energy of the Sun in an useful near-infrared one. In this case, a quantum cutting of the absorbed UV-Vis radiation by an activator ion can excite two sensitizer ions, giving rise to the possibility of emissions in the near-infrared region. In these processes, the evaluation of luminescence/heat generation rate is of outmost importance. The thermal lens (TL) and thermal mirror (TM) techniques are sensitive and important photothermal methods to quantitatively investigate the energy-conversion processes since they measure the fraction of the light energy converted into heat after the material being illuminated. In addition, these methods allow the determination of thermophysical properties like thermal diffusivity and thermal conductivity, relevant in the working condition since each degree of variation in the surrounding temperature the panel efficiency reduces about 1%.

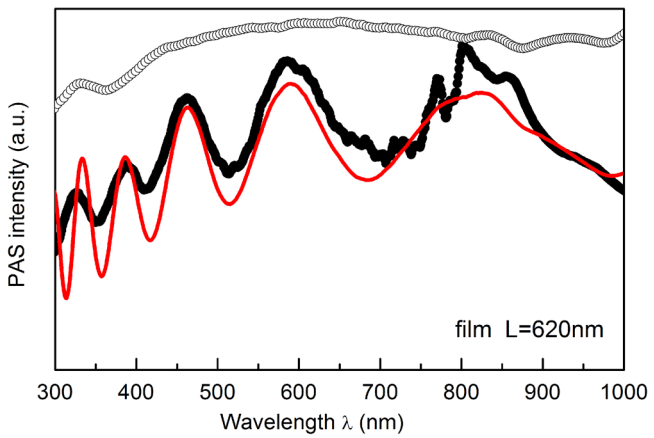

FIG. 12. Photoacoustic spectra (PAS) of the (o) c-Si substrate and (·) glass thin film deposited on the c-Si substrate. The solid line shows the PAS theoretical simulation using Eq. (9).

A. Brief introduction of thermal lens spectrometry

The term "thermal lens" comes from the fact that a lens-like optical element is created after a laser impinges on a semi-transparent liquid or solid sample. When a TEM_{00} Gaussian profile laser beam (the excitation beam) illuminates the sample, the sample is heated by the absorbed excitation laser energy, resulting in a radial temperature gradient. Since the refractive index of the sample changes with temperature, a radial refractive-index gradient is created, forming a lens-like optical element, the so-called thermal lens. The propagation of a TEM_{00} Gaussian laser beam (the probe beam) passing through the TL will be affected, causing the variation of the spot size and then intensity distribution of the probe beam. The information on the optical and thermophysical properties of the sample can be obtained by measuring these variations, including the fraction of energy converted into heat.

The experiment arrangement and theory of TL spectroscopy have both evolved considerably since it was first developed. Early experimental devices used one laser beam to excite and probe the TL. Hu and Whinnery demonstrated that a sensitive TL detection could be achieved using a converging lens to form a beam waist at one confocal distance (namely, Rayleigh length) before the sample.[122] Later, dual-beam experimental arrangements emerged, which used separate laser beams for exciting and probing the TL.[123] There are two kinds of dual-beam TL experimental arrangements. One is mode-matched, in which the spot sizes of the excitation and probe beams in the sample are the same. The other is mode-mismatched, wherein the spot sizes are different. The mode-mismatched arrangement was found to be more sensitive than the mode-matched one,[124] since in this arrangement the sample is usually positioned at the waist of a focused excitation beam, where the power density of the excitation beam and the thermally produced refractive-index gradient are at a maximum. Taking full advantage of geometric and spatial aspects of a mode-mismatched configuration, Marcano *et al.* maximized the TL signal using an expanded and collimated probe beam, while keeping the sample at the waist of a focused excitation beam.[125]

In a mode-mismatched dual-beam TL experiment, shown in Fig. 13, the probe beam propagates collinearly with the excitation beam and radiates continuously, and the illumination of the excitation beam is controlled by a shutter. After the shutter is opened at time $t = 0$, the time-resolved probe beam intensity (transient) $I_p(t)$ at its beam center at the detector plane is[126,127]

$$I_p(t) = I_p(0)\left(1-\frac{\theta_{\mathrm{TL}},}{2} \times \tan^{-1}\left\{\frac{2mV}{[(1+2m)^2+V^2][t_c/(2t)]+1+2m+V^2}\right\}^2\right), \tag{10}$$

with $\theta_{TL} = -\frac{P_e \beta l_s \varphi}{\lambda_p k_T}\frac{ds}{dT}$, $t_c = \omega_e^2/(4\alpha)$, $m = (\omega_{1p}/\omega_e)^2$, and $V = \frac{\pi\omega_{1p}^2}{\lambda_p}\left(\frac{1}{R_{1p}}+\frac{1}{Z_2}\right)$. Here, β, l_s, $\frac{ds}{dT}$, k_T, α, denote the absorption (attenuation) coefficient at the excitation beam wavelength λ_{ex}, sample thickness, thermo-optic coefficient (namely, ds/dT is the temperature coefficient of the optical path length) at the probe beam wavelength λ_p, thermal conductivity, and thermal diffusivity of the sample, respectively. φ is the rate (percentage) of the absorbed excitation beam energy converted into heat, given by[128]

$$\varphi = 1 - \eta\frac{\lambda_{ex}}{\langle\lambda_{em}\rangle}, \tag{11}$$

where $\langle\lambda_{em}\rangle$ is the average emission wavelength and η is the fluorescence quantum efficiency. ω_e and ω_{1p} are the spot sizes of the excitation and probe beams, respectively. t_c is a characteristic thermal time constant. R_{1p} and Z_2 are the radius of curvature of the probe beam at the sample location and the distance between the sample and the detector plane, respectively. $I_p(0)$ is the probe beam intensity at time $t = 0$. For liquid samples $ds/dT = dn/dT$.[129] The experiments can be done in the time resolved mode by both pulsed and/or CW lasers and in the steady-state conditions. The most used experimental setup configuration is shown in Fig. 14. It contains excitation and probe lasers, optical lenses and mirrors for beam divergence and spot sizes control, detectors for triggering and signal measurement. Further details can be found elsewhere.[130,131]

Figure 15 illustrates a TL transient obtained from a tellurite glass sample with a CW laser excitation at 514.5 nm and excitation power of 40 mW. The curve fitting with Eq. (10) provides two parameters, t_c and θ_{TL}, which are related to the thermophysical properties of the samples. When the sample is luminescent, the parameter θ_{TL}, provides the fraction of incident energy converted into heat (φ), expressed in Eq. (11).

When the measurement time $t \gg t_c$, the steady-state TL signal $S(\infty)$ can be defined as[126]

$$S(\infty) = \frac{I_p(\infty) - I_p(0)}{I_p(0)} = \left[1 - \frac{\theta_{TL}}{2}\tan^{-1}\left(\frac{2mV}{1+2m+V^2}\right)\right]^2 - 1. \tag{12}$$

Let $Q(m, V) = \frac{2mV}{1+2m+V^2}$, and if $\left|\frac{\theta_{TL}}{2}\tan^{-1}\left(\frac{2mV}{1+2m+V^2}\right)\right| \ll 1$, Eq. (12) becomes

$$S(\infty) \approx -\theta_{TL}\tan^{-1}[Q(m, V)]. \tag{13}$$

When $2m \gg 1$ and $2m \gg V^2$, $Q(m, V) \approx V$,[132] and Eq. (13) turns out to be

$$S(\infty) \approx -\theta_{TL}\tan^{-1}(V). \tag{14}$$

Equations (13) and (14) exhibit that the maximum steady-state TL signal is $S(\infty) \approx -\frac{\pi}{2}\theta_{TL}$.

A steady-state TL experiment arrangement can be optimized. To find the roots for $\frac{dQ(m, V)}{dZ_2} = \frac{dQ(m, V)}{dV}\frac{dV}{dZ_2} = 0$, let $\frac{dQ(m, V)}{dV} = 0$, which leads to the optimized V,[133]

$$V_{opt} = \pm\sqrt{1+2m}. \tag{15}$$

The $\pm$ solutions correspond to the situations where the sample is positioned, respectively, after and before the probe beam waist. When the probe beam is a collimated Gaussian laser beam,

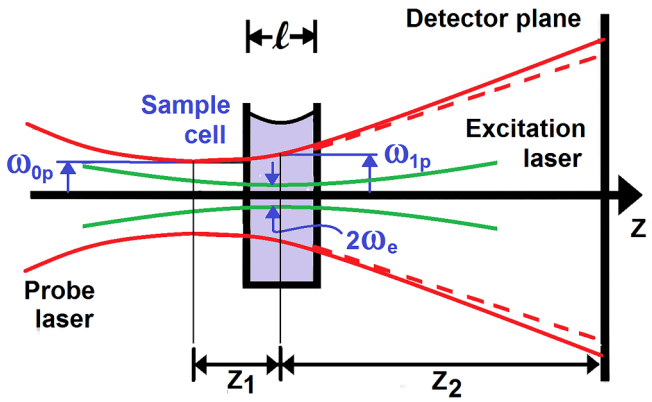

FIG. 13. A schematic diagram of the geometric positions of laser beams in a mode-mismatched dual-beam TL experimental arrangement.

$R_{1p} \to \infty$, and, therefore,

$$V = \frac{\pi\omega_{1p}^2}{\lambda_p}\left(\frac{1}{R_{1p}} + \frac{1}{Z_2}\right) = \frac{\pi\omega_{1p}^2}{\lambda_p Z_2}. \tag{16}$$

Combining Eqs. (15) and (16), one may find the optimized Z_2 for the steady-state TL signal $S(\infty)$ with a collimated Gaussian probe laser beam to be

$$Z_{2opt} = \frac{\pi\omega_{1p}^2}{\lambda_p\sqrt{1+2m}}. \tag{17}$$

The model proposed in Eq. (10) for the TL signal intensity works very well in the case of low optical absorption samples, small phase shift, and assuming negligible heat flux from the sample to the adjacent medium. In order to overcome these limitations, more complete models were recently proposed.[134–137] Also, the description of the optical path in solid samples presents a simple form only in the plane stress or plane strain approximation, which limits the application for very thin or thick samples. A generalized theoretical model was obtained for the optical path change overcoming the limitation of plane stress or plane strain approximations. The obtained expression of the optical path change is related to the temperature profile in a relatively simple manner for all classes of absorbing optical materials, correlating optical path change to thermo-optical-mechanical properties of solid materials.[138,139]

Under the possibility of using the TL technique for quantitative measurements and also due to its high sensitivity, this method is useful to evaluate the fraction of the absorbed light energy that is converted to heat in both real solar cells and their built-in materials, as follows.

B. Energy transfer and activator-sensitizer rate equations for hybrid solar cells

Besides the study of solar cell physical process, the photothermal techniques have been successful applied to study the spectral conversion of solar spectra, as illustrated in Fig. 5. Normally, silicon absorbs only a small part of the total incident solar energy due to the spectral mismatch between its absorption band and the solar spectra [Fig. 5(a)]. The practical efficiency of silicon solar cells would be much improved by an efficient so-called downconversion (DC) of the UV-visible part of the solar spectrum to the near-infrared (NIR) region considering that silicon has maximal response at ~1.1 eV (~1000 nm). Similarly, an upconversion (UC) process would convert low energy photons to higher energies, since these below bandgap energy photons are not absorbed by silicon. Rare earth (RE)-doped materials are known for their capability of

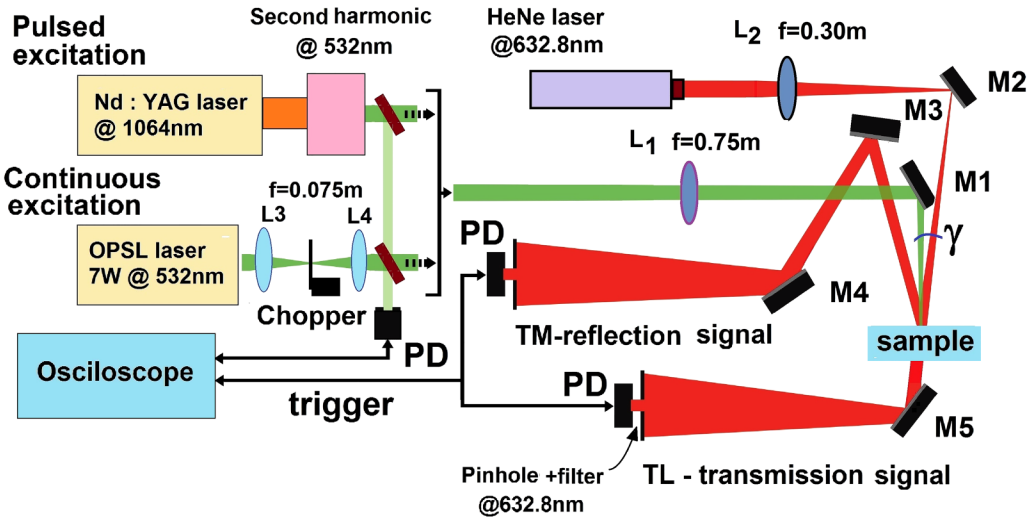

FIG. 14. Experimental setups for CW or pulsed lasers in the mode-mismatched configuration for the TL and TM methods.[107,108]

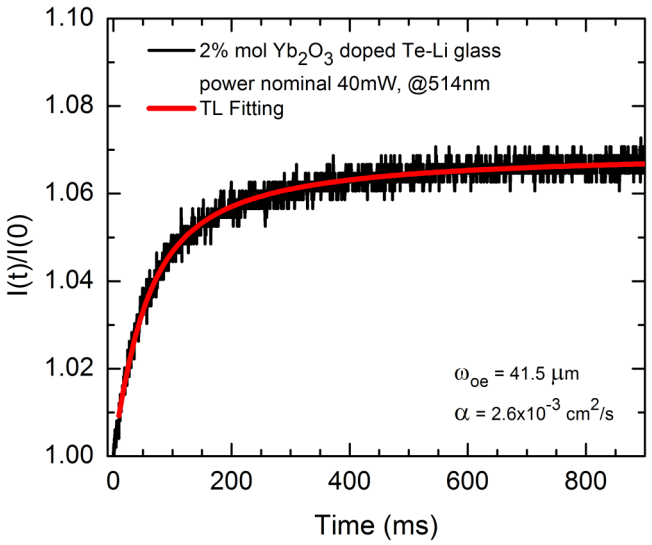

FIG. 15. Characteristic TL transient signal for a tellurite glass sample.

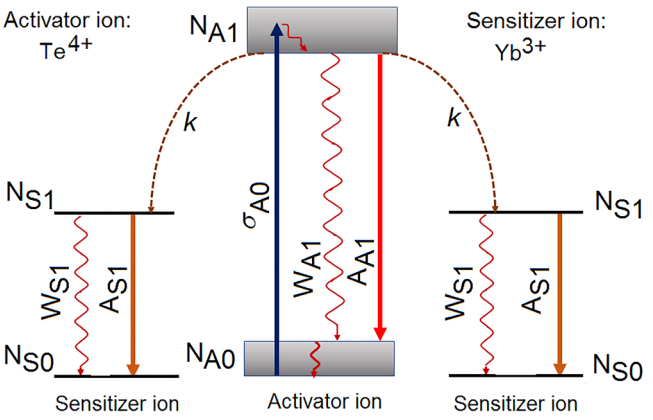

FIG. 16. Partial energy level diagram of an activator (Te^{4+}) ion and two sensitizer (Yb^{3+}) ions. The solid arrows and the wavy lines represent the radiative and non-radiative transitions, respectively. The dash arrows indicate the cooperative energy transfer (CET) mechanism for the near infrared quantum cutting emission under UV-blue excitation.

DC and UC due to energy transfer processes by a pair of ions. An example of DC in a RE–Yb^{3+} spectral converter is the co-doped aluminosilicate glasses promoting emission around 980 nm, as illustrated in Fig. 5(b).[32,117,140] One RE ion (Eu^{2+} or Nd^{3+}) acts as an absorption center and transfer energy to Yb^{3+}. In this case, Eu^{2+} and Nd^{3+} were chosen to efficiently absorb the UV and visible light, respectively, as shown by the purple and green absorption spectra in Fig. 5(b). Yb^{3+} is the best acceptor ion for silicon solar cells, because its emission (~980 nm) matches well to the Si absorption (bandgap ~1.1 eV). In this DC processes, Eu^{2+} and Nd^{3+} are called activators and Yb^{3+} the sensitizer ions. In this paper, a few examples will be presented showing that photothermal techniques can have a crucial role in the quantitative characterization of these processes.

Before considering the use of the TL technique to study energy conversion in these spectral converter systems, the rate equations involving the energy transfer processes in DC luminescence are shown for the Te^{4+}-Yb^{3+} co-doped tellurite glasses. Subsequently, the Nd^{3+}-Yb^{3+} co-doped low silica calcium aluminosilicate glasses (LSCAS) are studied with the measurement made with the TM technique, which differs from TL by detecting the probe beam reflection on the sample surface instead of its transmission.

Figure 16 schematizes a partial energy level diagram for an activator/sensitizer ions pair, in which a CET mechanism is possible. As can be noticed, the DC mechanism is strongly correlated with non-radiative transitions (wavy lines), which are responsible for heating the material. In this sense, TL and TM methods have been used to quantify the fraction of the absorbed energy that is converted into heat, φ, from where the efficiencies of the DC process can be monitored.[141,142]

As mentioned before, among the REs widely investigated, Yb^{3+} has been explored as the main sensitizer, mainly due to its broad emission band at around 980 nm, which corresponds to the maximum spectral response range of Si solar cells.[51] Depending on the activator, the energy absorbed is governed by the 4f–4f parity forbidden transitions, whereby only a small portion of the solar spectrum is involved in the spectral conversion process. Efforts have been made to use activator ions that exhibit wide absorption band in the UV-Vis region, as such those governed by the 4f–5d allowed transitions (Ce^{3+} and Eu^{2+}, for instance),[143,144] or by transition metals like Cr^{3+} and Te^{4+}.[145,141] For these materials, the CET efficiencies are known to be higher due to their energy states configurations. The scheme in Fig. 16 can be used to represent different activator/sensitizer ions pair, such as Ce^{3+}/Yb^{3+},[143] Eu^{2+}/Yb^{3+},[144] and Te^{4+}/Yb^{3+}.[141]

With the figure, it is possible to realize that an efficient CET process can contribute reducing the fraction of the absorbed energy that is converted into heat, mainly when the activator ion has not high luminescence quantum efficiency. Accordingly, an increase in the sensitizer concentration ion can contribute to this reduction, turning the system interesting to be applied in hybrid solar cells to increase the conversion efficiency of the solar energy into the electric one.

Few studies had used PT methods to verify the thermal dependence on activator/sensitizer ions pairs. In order to obtain an expression for the fraction of the absorbed energy that is converted into heat (φ), Fig. 16 is considered to write the following rate equations for the populations in the excited states of the activator (N_{A1}) and sensitizer (N_{S1}) ions:

$$\frac{dN_{A1}}{dt} = \left(\frac{I}{E_{exc}}\right)\sigma_{A0}N_{A0} - A_{A1}N_{A1} - kN_{A1}(N_{S0})^2 - W_{A1}N_{A1}, \tag{18a}$$

$$\frac{dN_{S1}}{dt} = 2kN_{A1}(N_{S0})^2 - A_{S1}N_{S1} - W_{S1}N_{S1}, \tag{18b}$$

with σ_{A0} being the absorption cross section from the fundamental state of the activator ion, I is the pump intensity and E_{exc} the excitation energy, N_{A0} (N_{S0}) and N_{A1} (N_{S1}) the population at the fundamental and excited states of the activator (sensitizer) ion, respectively, A_i and W_i are the radiative and non-radiative decay rates for each "i" state, and k is the probability of CET. The populations of N_{A1} and N_{S1} excited states were obtained under steady-state conditions, giving

$$N_{A1} = \left(\frac{I}{E_{exc}}\right)\frac{1}{A_{A1} + k(N_{S0})^2 + W_{A1}}\sigma_{A0}N_{A0}, \tag{19a}$$

$$N_{S1} = \left(\frac{I}{E_{exc}}\right)\frac{2k(N_{S0})^2}{[A_{A1} + k(N_{S0})^2 + W_{A1}](A_{S1} + W_{S1})}\sigma_{A0}N_{A0}. \tag{19b}$$

The total heat (H) generated in the sample is determined adding all the non-radiative decays indicated in Fig. 16, Ws, as follows:

$$H = (E_{exc} - E_{A1\rightarrow A0})\left(\frac{I}{E_{exc}}\right)\sigma_{A0}N_{A0} + W_{A1}N_{A1}E_{A1\rightarrow A0} + 2W_{S1}N_{S1}E_{S1\rightarrow S0}, \tag{20}$$

in which $E_{A1\rightarrow A0}$ and $E_{S1\rightarrow S0}$ are the energy of the radiative transitions in the activator and sensitizer ions, respectively. By substituting Eq. (19) into (20), the fraction of the absorbed energy converted into heat can be written as

$$\varphi = \frac{H}{N_{A0}I\sigma_{A0}} = 1 - (\eta_{A1} + \eta_{CET})\frac{\lambda_{ex}}{\langle\lambda_{em}\rangle_{A1}} + 4\eta_{CET}(1 - \eta_{S1})\frac{\lambda_e}{\langle\lambda_{em}\rangle_{S1}}. \tag{21}$$

In this equation, the excitation and emission energies were written in terms of their wavelengths (λ_{ex} and λ_{em}, respectively), and the efficiencies were defined as

$$\eta_{A1} = \frac{A_{A1}}{A_{A1} + k(N_{S0})^2 + W_{A1}}, \tag{22a}$$

$$\eta_{CET} = \frac{k(N_{S0})^2}{A_{A1} + k(N_{S0})^2 + W_{A1}}, \tag{22b}$$

and

$$\eta_{S1} = \frac{A_{S1}}{A_{S1} + W_{S1}}. \tag{22c}$$

With this approach, measuring φ values with PT methods, the sample luminescence quantum efficiency can be determined.[128]

C. TL technique for measuring the absorbed energy converted into heat (φ) in Te^{4+}/Yb^{3+} co-doped tellurite glass

In order to verify Eq. (21), the fraction of the absorbed energy converted into heat (φ) was calculated for the Te^{4+}/Yb^{3+} co-doped tellurite glass, and the obtained result is plotted in Fig. 17 as a function of the Yb^{3+} sensitizer ion concentration. There is a good agreement between the calculated values and the experimental data determined by the TL method.[141] As expected, a reduction in the heat generation as a function of the Yb^{3+} concentration was observed as a consequence of energy transfer from the Te^{4+} to the Yb^{3+}, as illustrated in Fig. 16.

D. TM for measuring the absorbed energy converted to heat (φ) in Nd^{3+}/Yb^{3+} co-doped LSCAS

Another rare-earth co-doped system with efficient DC mechanisms is the Nd^{3+}/Yb^{3+}. Figure 18 schematizes the energy level diagram for this system. As noticed, one UV-blue excitation photon is absorbed by the activator ion followed by different ways to transfer this absorbed energy to two sensitizers, as indicated by dashed arrows. These cross-relaxation mechanisms, CRs, can reduce the non-radiative rates which, consequently, affect the fraction of the absorbed energy converted into heat in the material increasing the DC luminescence to ~980 nm.

In order to obtain an expression for the fraction of the absorbed energy that is converted into heat (φ), considering all the non-radiative and radiative transitions indicated in Fig. 18, the rate equations for the Nd^{3+}/Yb^{3+} co-doped system was solved, following

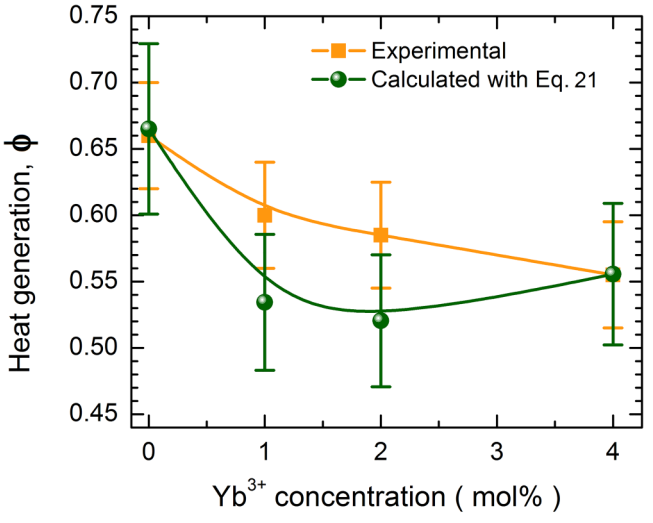

FIG. 17. Heat generation for Te^{4+}/Yb^{3+} co-doped tellurite glass as a function of the Yb^{3+} concentration. The experimental results were obtained by exciting the glasses at 360 nm, and the calculated data were obtained with the literature values:[141] $\langle\lambda_{em}\rangle_{A1} = \langle\lambda_{em}\rangle_{Te} = 645$ nm, $\langle\lambda_{em}\rangle_{S1} = \langle\lambda_{em}\rangle_{Yb} = 1003$ nm, and $\eta_{A1} = \eta_{Te} = 0.64$. The $\eta_{CET} = 0.28$, 0.38, and 0.86 and $\eta_{S1} = \eta_{Yb} = 0.94$, 0.88, and 0.70 were used for the samples with 1, 2, and 4 mol. % of Yb^{3+}, respectively.

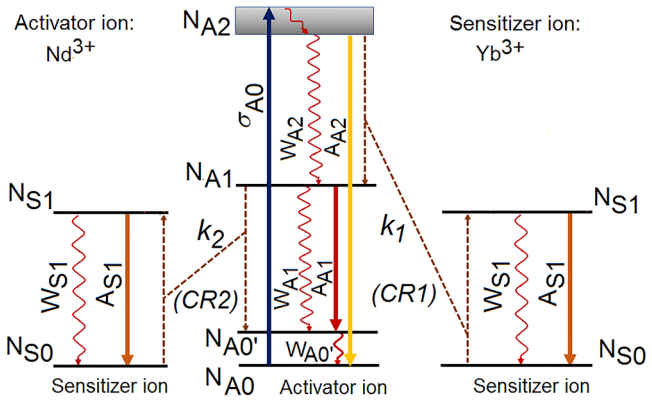

FIG. 18. Partial energy level diagram of the activator (Nd^{3+}) and two sensitizer (Yb^{3+}) ions. The solid arrows and the wavy lines represent the radiative and non-radiative transitions, respectively. The dashed arrows indicate the cross relaxation (CR) mechanism.

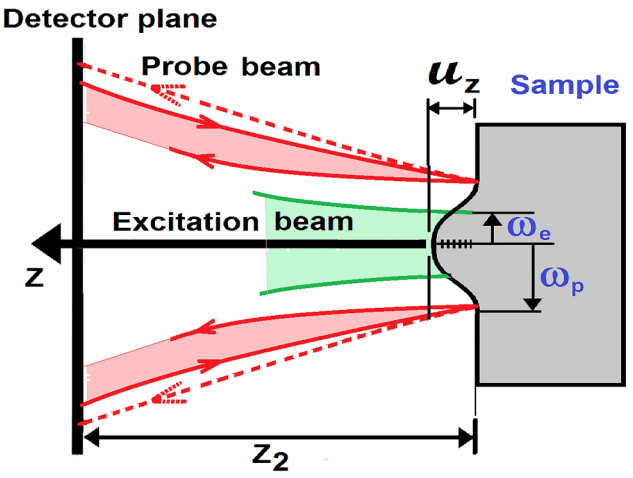

FIG. 19. A schematic diagram of the geometric positions of laser beams in a mode-mismatched dual-beam TM experimental arrangement.

the steps described above, and the obtained results are (for complete detail on the math procedure and the terms in the equation, please see S1 in the supplementary material)

$$\varphi = 1 - \eta_{A2}\frac{\lambda_{ex}}{\langle\lambda_{em}\rangle_{A2\to A0}} - \eta_{k1}\frac{\lambda_{ex}}{\langle\lambda_{em}\rangle_{A2\to A1}} - (\eta_{k2}+\eta_{A1})\frac{\lambda_{ex}}{\langle\lambda_{em}\rangle_{A1\to A0'}} + [\eta_{k1}+\eta_{k2}(1-\eta_{A2})]2(1-\eta_{S1})\frac{\lambda_{ex}}{\langle\lambda_{em}\rangle_{S1\to S0}}. \quad (23)$$

To test this system, we used Nd^{3+}/Yb^{3+} co-doped LSCAS glass and the thermal mirror (TM) technique, as follows in the next section.

E. Thermal mirror background

In addition to the TL technique, another pump-probe photothermal method was recently developed taking into account the use of a laser-induced optical path change. Instead of monitoring the transmitted probe beam through the sample, this method monitors the probe beam reflected off on the sample surface. In allusion to TL term, this method was nominated as thermal mirror (TM).[146–149] The TM effect manifests when a laser beam shines on a material surface and part of the absorbed optical energy is converted into heat. The heating presents a radial gradient, followed by a displacement profile. The sample surface displacement induces a phase shift on the probe beam wavefront reflected off on the surface, as presented in Fig. 19.

TM is generally applied in mode-mismatched dual-beam experiments. The probe beam is continuously radiating on the sample and propagates almost collinearly with the excitation beam, whose exposure is controlled by a mechanical shutter. Only the central portion of the probe beam is monitored by a detector in the far field. After the shutter is opened at time t = 0, the time-resolved probe beam intensity is evaluated. The method was already presented in different experimental setups, using Gaussian and top-hat radial intensity distribution,[32,135,150,151] with continuous (CW) and pulsed lasers.[130,152–154] Also, the theory was extensively studied, approaching different experimental conditions, and different kinds of materials.[151,155–159]

Thermal mirror follows the same theoretical procedure used to obtain the TL model. The temperature profile is determined by solving the heat conduction differential equation; however, TM has the advantage of being applicable also in high absorbing materials (opaque materials). In this sense, choosing the most adequate source term, three different optical absorption domains can be obtained solving the heat conduction differential equation, the low absorption approximation (LAM), the Beer's law absorption attenuation, and the high absorption approximation (HAM).[151]

The temperature change induces a deformation in the sample surface, which can be described by the thermoelastic equation in quasistatic approximation, given by[160]

$$(1-2\nu)\,\nabla^2\boldsymbol{u} + \nabla(\nabla.\boldsymbol{u}) = 2(1+\nu)\,\alpha_T\,\nabla T(r,z,t), \quad (24)$$

with the boundary conditions at the surface, $\sigma_{rz}|_{z=0} = 0$ and $\sigma_{zz}|_{z=0} = 0$, which are the normal stress components. The displacement vector is defined by $\boldsymbol{u}$, α_T is the linear thermal expansion coefficient, and ν is the Poisson ratio of the material.

Since the method uses cylindrically symmetrical beams, the solution may be obtained in cylindrical coordinates, by introducing the scalar displacement potential and the Love function.[151] A full analytical model is not available; however, a simple model can be achieved by regarding some experimental configurations, and sample geometries. For instance, considering a sample much larger than the excitation beam, and in the low absorption regime, the

displacement in z is obtained,

$$u_z\,(r,0,t) = -\alpha_T\,(1+\nu)\,T_0 \int_0^t \left(\frac{2\pi/\omega_e^2}{1+2\tau/t_c}\right)^{1/2} \times \exp\left(\frac{-r^2/\omega_e^2}{1+2\tau/t_c}\right) I_0\left(\frac{r^2/\omega_e^2}{1+2\tau/t_c}\right) d\tau, \quad (25)$$

with

$$T_0 = \frac{P_e \beta}{\pi c_p \rho}\varphi, \quad (26)$$

where the parameters are the same as specified in the TL model. Here c_p and ρ are the specific heat and density of the sample, respectively, and $I_n(z)$ is the n-order modified Bessel function of the first kind.

The sample surface displacement acts as an optical element, causing a phase shift to the reflected probe beam $\Phi = (4\pi/\lambda_p)\,u_z(r,0,t)$, which in the case of low absorption model is given by[149,151]

$$\Phi_{LAM}\,(g,t) = \theta_{TM}\sqrt{2\pi}\,\omega_e \left\{ \exp\left(\frac{-gm}{1+2t/t_c}\right)(1+2t/t_c)^{-1/2} \times \left[(1+2gm+2t/t_c)\,I_0\left(\frac{gm}{1+2\tau/t_c}\right) + 2gmI_1\left(\frac{gm}{1+2\tau/t_c}\right)\right] - \exp(-gm)[(1+2gm)\,I_0\,(gm) + 2gmI_1\,(gm)] \right\}, \quad (27)$$

where $g = (r/\omega_p)^2$, and

$$\theta_{TM} = -\frac{P_e\,\beta\,\alpha_T\,(1+\nu)}{\lambda_p k}\varphi, \quad (28)$$

which correlates the thermal, optical, and mechanical properties of the sample, influencing directly in the probe beam intensity variation amplitude, while the characteristic time behavior depends on the sample thermal diffusivity. The probe beam intensity variation can be obtained by carrying out numerical integration over g as

$$\frac{I(t)}{I(0)} = (1+V^2)\left|\int_0^\infty \exp[-(1+iV)g - i\Phi_{LAM}\,(g,t)]dg\right|^2. \quad (29)$$

This model was already used in several transparent materials from polymers[130] to optical ion-doped glasses.[150,161] In these systems, the technique is capable of accessing the fluorescence quantum efficiency of a determined ion inserted into the host.

Here, the TM technique is applied to measure the fraction of generated heat in Nd^{3+}/Yb^{3+} co-doped LSCAS. The glasses were prepared with the nominal composition (wt. %) (46.9−x/2) CaO + (41.0−x/2) Al_2O_3 + 7SiO_2 + 4.1MgO + 1 Nd_2O_3 + x Yb_2O_3, using high-purity grade oxides, better than 99.99%. The concentrations of Yb_2O_3 were x = 0, 1, 2, 4, 6, and 8. Details of the sample synthesis can be found elsewhere Refs. 32 and 41.

TM experiments were performed using a conventional setup at room temperature similar to that of Fig. 14.[153] The samples were excited at two different wavelengths of an Argon laser, 351 or 514.5 nm. The thermal diffusivity and the parameter θ_{TM} were obtained from regression using Eq. (29) for each sample. Variables like V, g, and m in this equation and in Eq. (28) are from the experimental setup configuration and are measured separated.[149] The values obtained for the thermal diffusivity were constant for all samples, giving an average value of $\alpha = 5.5 \times 10^{-3}$ cm^2/s, in good agreement with previously works.[153,161] From θ_{TM}, it is possible to access the fraction of absorbed energy converted into heat (φ) as a function of Yb_2O_3 concentration, as presented in Fig. 20.

The results show a decrease of the heat generation from the sample doped only with Nd^{3+} to the sample co-doped with Nd and 1 wt. % of Yb_2O_3, for both excitation wavelengths. However, adding more Yb^{3+} into the glass increased the heat generation due to ion–ion interactions that decrease the luminescence quantum yield. These experimental results (closed circles) were compared to Eq. (23) (open circles), which are also presented in Fig. 20. The proposed model to derive the population rate equations is presented in the supplementary material, S1, and showed good agreement with the experimental observation.

The surface displacement obtained by the TM method was already compared to direct laser-induced displacement measurements,[159,162] by atomic force microscopy (AFM). Here, we present

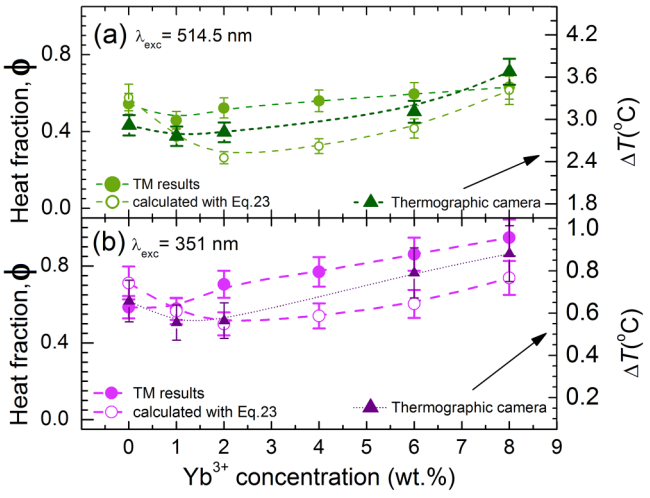

FIG. 20. Heat generation for Nd^{3+}/Yb^{3+} co-doped LSCAS glass as a function of the Yb^{3+} concentration. The TM experimental results were obtained by exciting the glasses at (a) 514.5 and (b) 351 nm (closed circles), and the calculated data (open circles) were obtained with the literature values:[32] $\langle\lambda_{em}\rangle_{Nd}$ = 1077 nm, $\langle\lambda_{em}\rangle_{Yb}$ = 1011 nm, and η_{Nd} = 0.88. The η_{CET} = 0.48, 0.68, 0.82, 0.89, and 0.92 and η_{Yb} = 0.97, 0.98, 0.83, 0.70, and 0.48 were used for the samples with 1, 2, 4, 6, and 8 wt. % of Yb^{3+}, respectively. A direct temperature change is also presented (closed triangles), in order to compare the tendency of the heat fraction with the increase of Yb^{3+} concentration.

the first comparison of the heat fraction evolution with the increase of Yb^{3+} obtained by the TM method with a direct temperature change measurement. The direct temperature change was obtained by a thermographic imaging infrared camera (InfraTec - ImageIR 7300), which presents a measured temperature resolution of 0.002 K. Despite direct measurement of the temperature is a very difficult task in photothermal methods, since the temperature change is very small and localized in the region close to the excited area, the results are in good agreement and showed a decrease of the heat generation in the sample co-doped with 1 wt. % of Nd_2O_3 and 1 wt. % of Yb_2O_3, which fundamentally evidences an efficient energy transfer from the Nd^{3+} to the Yb^{3+} due to the coupling between these ions, and encourages the search of materials capable of converting the solar spectral energy distribution in the UV and visible to the near-infrared, more suitable to the Si solar cells.

VI. CONCLUSION AND PERSPECTIVES OF FUTURE WORK

In conclusion, this Tutorial presents an up-to-date description of the photoacoustic and photothermal methods and their advantages to determine the heat generation in solar cells and their built-in materials. Potential application of these methods for studies evaluating the heat generation in the downconversion processes in co-doped spectral converters is an important tool toward the measurements of parameters related to the development of the hybrid solar cells and, consequently, the determination of their photovoltaic efficiencies. Quantitative measurements of both fluorescence quantum efficiency and carrier photoproduction as well as of thermophysical parameters are probably the most important and unique characteristics of these methods for this area. The challenges in future works are to overcome the limitation of preparing the spectral converters as thin films over solar cells and the thin film characterization. The latter presents additional issues to be considered in terms of quantitative photothermal measurements since the fundamental of the TL and TM techniques is the measurement of the excitation laser-induced optical path length change and surface deformation, which, in usual materials, are directly connected with the localized temperature profile, described by the thermo diffusion and thermoelastic equations.[151]

In an optically excited semiconductor, an additional contribution comes from the coupling of electronic and thermal effects, where the de-excitation process could work as a heat source to the sample. However, it was shown for the case of bulk samples that the TM technique decouples thermal effects in semiconductors and presents low sensitivity to the electronic effects.[158]

In the case of thin-films on a substrate, in addition to the contribution of the electronics effects, an additional limitation for TM and TL techniques is the absence of an analytical or semi-analytical solution for the diffusion and thermoelastic equations in this coupled system. Notwithstanding, qualitative results could be obtained in the thin film characterization, and quantitative results restricted to numerical analysis.

SUPPLEMENTARY MATERIAL

See the supplementary material S1 for the rate equations for the Nd^{3+}-Yb^{3+} co-doped activator and sensitizers ions, respectively, and the analytical expression for the fraction of the absorbed energy converted into heat (φ), considering all the non-radiative and radiative transitions indicated in Fig. 18.

DEDICATION

This work is dedicated to Professor Andreas Mandelis for his notable achievements and multifaceted seminal contributions to the fields of photothermal, photoacoustic, and diffusion waves. Professor Mandelis' outstanding experimental and theoretical contributions to the development of different experimental methods resulted in many pioneering theoretical and experimental achievements, new methodologies, devices, and measurements spanning and spawning an exceptionally wide range of disciplines.

ACKNOWLEDGMENTS

The authors acknowledge support from the Brazilian agencies Coordenação de Aperfeiçoamento de Pessoal de Nível Superior (CAPES), Conselho Nacional de Desenvolvimento Científico e Tecnológico (CNPq), Fundação Araucária (FA), Financiadora de Estudos e Projetos (FINEP), Fundação de Apoio ao Desenvolvimento do Ensino, Ciência e Tecnologia do Estado de Mato Grosso do Sul (FUNDECT) and Agência Nacional de Energia Elétrica (ANEEL), Projeto P&D 2866-0466/2017-Código ANEEL for financial support of this work.

AUTHOR DECLARATIONS

Conflict of Interest

The authors have no conflicts to disclose.

DATA AVAILABILITY

The data that support the findings of this study are available from the corresponding author upon reasonable request.

REFERENCES

[1]A. E. Becquerel, Comptes Rendus **9**, 145 (1839).
[2]A. E. Becquerel, Comptes Rendus **9**, 561 (1839).
[3]T. J. Seebeck, *Ueber Den Magnetismus Der Galvanischen Kette in Den Abhandlungen Der Königlichen Akademie* (Georg Reimer, Berlin, 1822).
[4]E. S. Barr, Am. J. Phys. **28**, 42 (1960).
[5]A. W. Copeland, O. D. Black, and A. B. Garrett, Chem. Rev. **31**, 177–226 (1942).
[6]W. Smith, Nature **7**, 361 (1873).
[7]Society of Telegraph Engineers, *Journal of the Society of Telegraph Engineers: Including Original Communications on Telegraphy and Electrical Science* (Published under the supervision of the Editing Committee, 1877).
[8]H. Hertz, Äber Sehr Schnelle Elektrische Schwingungen. Vier Arbeiten (1887–1889) (Deutsch, 1996).
[9]W. G. Adams, Proc. R. Soc. London **24**, 163 (1876).
[10]R. Sabine, Nature **17**, 512 (1878).
[11]A. G. Bell and S. Tainter, US235,497 (14 December 1880).
[12]A. G. Bell, Am. J. Sci. **s3-20**, 305 (1880).
[13]A. G. Bell, Science **os-2**, 242 (1881).
[14]C. E. Fritts, Am. J. Sci. **s3-26**, 465 (1883).
[15]W. Hallwachs, Ann. Phy. Chemie **269**, 301 (1888).
[16]M. A. Stoletow, Lond. Edinb. Dublin Philos. Mag. J. Sci. **26**, 317 (1888).
[17]L. Nobili, Ann. Phy. Chem. **96**, 245 (1830).
[18]E. Weston, US389124 (4 September 1888).
[19]A. Einstein, Ann. Phys. **322**, 132 (1905).

[20]R. S. Ohl, US2,402,662 (25 June 1946).
[21]D. M. Chapin, C. S. Fuller, and G. L. Pearson, J. Appl. Phys. **25**, 676 (1954).
[22]D. M. Chapin, B. Ridge, C. S. Fuller, Chatham, and G. L. Pearson, US2,780,765 (5 February 1957).
[23]P. J. Hillson and E. K. Rideal, Proc. R. Soc. London, A **216**, 458 (1953).
[24]W. W. Anderson and Y. G. Chai, Energy Convers. **15**, 85 (1976).
[25]G. Hodes, J. Manassen, and D. Cahen, Nature **261**, 403 (1976).
[26]G. Hodes, J. Manassen, and D. Cahen, J. Appl. Electrochem. **7**, 181 (1977).
[27]J. Manassen, D. Cahen, G. Hodes, and A. Sofer, Nature **263**, 97 (1976).
[28]J. Manassen, G. Hodes, and D. Cahen, J. Electrochem. Soc. **124**, 532 (1977).
[29]G. Hodes, D. Cahen, and J. Manassen, Nature **260**, 312 (1976).
[30]S. Almosni, A. Delamarre, Z. Jehl, D. Suchet, L. Cojocaru, M. Giteau, B. Behaghel, A. Julian, C. Ibrahim, L. Tatry, H. Wang, T. Kubo, S. Uchida, H. Segawa, N. Miyashita, R. Tamaki, Y. Shoji, K. Yoshida, N. Ahsan, K. Watanabe, T. Inoue, M. Sugiyama, Y. Nakano, T. Hamamura, T. Toupance, C. Olivier, S. Chambon, L. Vignau, C. Geffroy, E. Cloutet, G. Hadziioannou, N. Cavassilas, P. Rale, A. Cattoni, S. Collin, F. Gibelli, M. Paire, L. Lombez, D. Aureau, M. Bouttemy, A. Etcheberry, Y. Okada, and J. F. Guillemoles, Sci. Technol. Adv. Mater. **19**, 336 (2018).
[31]B. L. Allsopp, R. Orman, S. R. Johnson, I. Baistow, G. Sanderson, P. Sundberg, C. Stålhandske, L. Grund, A. Andersson, J. Booth, P. A. Bingham, and S. Karlsson, Prog. Photovolt.: Res. Appl. **28**, 1187 (2020).
[32]L. J. Borrero-González, L. A. O. Nunes, G. S. Bianchi, F. B. G. Astrath, and M. L. Baesso, J. Appl. Phys. **114**, 013103 (2013).
[33]L. J. Borrero-González, L. A. O. Nunes, J. L. Carmo, F. B. G. Astrath, and M. L. Baesso, J. Lumin. **145**, 615 (2014).
[34]J. Yue, Y. Xiao, Y. Li, G. Han, Y. Zhang, and W. Hou, Org. Electron. **43**, 121 (2017).
[35]S. K. Karunakaran, C. Lou, G. M. Arumugam, C. Huihui, and D. Pribat, Solar Energy **188**, 45 (2019).
[36]X. Luo, J. Y. Ahn, and S. H. Kim, Solar Energy **178**, 173 (2019).
[37]A. Tombak, T. Kilicoglu, and Y. S. Ocak, Renew. Energy **146**, 1465 (2020).
[38]R. Elleuch, R. Salhi, J.-L. Deschanvres, and R. Maalej, J. Appl. Phys. **117**, 055301 (2015).
[39]C. Ma, H. Guo, X. Wang, Z. Chen, Q. Cang, X. Jia, Y. Li, N. Yuan, and J. Ding, Solar Energy **193**, 275 (2019).
[40]T. Carlier, S. Saitzek, F. O. Méar, J.-F. Blach, A. Ferri, M. Huvé, and L. Montagne, Appl. Surf. Sci. **397**, 13 (2017).
[41]A. Steimacher, N. G. C. Astrath, A. Novatski, F. Pedrochi, A. C. Bento, M. L. Baesso, and A. N. Medina, J. Non-Cryst. Solids **352**, 3613 (2006).
[42]J. Day, S. Senthilarasu, and T. K. Mallick, Renew. Energy **132**, 186 (2019).
[43]L. Hu and A. Mandelis, J. Appl. Phys. **129**, 091101 (2021).
[44]T. Mongstad, A. Thøgersen, A. Subrahmanyam, and S. Karazhanov, Sol. Energy Mater. Sol. Cells **128**, 270 (2014).
[45]Q. Yang, X. A. Zhang, A. Bagal, W. Guo, and C.-H. Chang, Nanotechnology **24**, 235202 (2013).
[46]T. Saga, NPG Asia Mater. **2**, 96 (2010).
[47]A. Bosio, S. Pasini, and N. Romeo, Coatings **10**, 344 (2020).
[48]H. Lian, Z. Hou, M. Shang, D. Geng, Y. Zhang, and J. Lin, Energy **57**, 270 (2013).
[49]W. Naim, V. Novelli, I. Nikolinakos, N. Barbero, I. Dzeba, F. Grifoni, Y. Ren, T. Alnasser, A. Velardo, R. Borrelli, S. Haacke, S. M. Zakeeruddin, M. Graetzel, C. Barolo, and F. Sauvage, JACS Au **1**, 409 (2021).
[50]S. W. Glunz, R. Preu, and D. Biro, Compr. Renew. Energy **1**, 353–387 (2012).
[51]M. B. de la Mora, O. Amelines-Sarria, B. M. Monroy, C. D. Hernández-Pérez, and J. E. Lugo, Sol. Energy Mater. Sol. Cells **165**, 59 (2017).
[52]A. Rosencwaig and A. Gersho, J. Appl. Phys. **47**, 64 (1976).
[53]A. Rosencwaig, *Photoacoustic and Photoacoustic Spectroscopy, Chemical Analysis* (Wiley, New York, 1980).
[54]H. Vargas and L. C. M. Miranda, Phys. Rep. **161**, 43 (1988).
[55]C. Haisch, Meas. Sci. Technol. **23**, 012001 (2012).
[56]S. S. S. Choi, B. Lashkari, A. Mandelis, J. Son, N. Alves-Kotzev, S. F. Foster, M. Harduar, and B. Courtney, J. Biomed. Opt. **24**(6), 066003 (2019).
[57]D. Cahen, Appl. Phys. Lett. **33**, 810 (1978).
[58]D. Cahen and S. D. Halle, Appl. Phys. Lett. **46**, 446 (1985).
[59]H. Flaisher, M. Wolf, and D. Cahen, J. Appl. Phys. **66**, 1832 (1989).
[60]B. Büchner, D. Cahen, and M. Wolf, Proc. SPIE-Int. Soc. Opt. Eng. **1149**, 1–8 (1989).
[61]S. M. N. Mello, C. C. Ghizoni, L. C. M. Miranda, and H. Vargas, J. Appl. Phys. **61**, 5176 (1987).
[62]H. L. Riette, L. C. M. Miranda, and H. Vargas, Appl. Phys. A **44**, 219 (1987).
[63]D. Cahen, B. Büchner, F. Decker, and M. Wolf, IEEE Trans. Electron Devices **37**, 498 (1990).
[64]D. Cahen, P.-E. Nordal, and S. O. Kanstad, Appl. Phys. Lett. **49**, 1351 (1986).
[65]I. F. Faria, C. C. Ghizoni, L. C. M. Miranda, and H. Vargas, J. Appl. Phys. **59**, 3294 (1986).
[66]H. Flaisher and D. Cahen, IEEE Trans. Ultrason. Ferroelect. Freq. Control **33**, 622 (1986).
[67]D. Cahen and S. Otto Kanstad, Solar Cells **25**, 155 (1988).
[68]B. Büchner, N. Cella, and D. Cahen, Isr. J. Chem. **38**, 223 (1998).
[69]A. Badawi, J. Mater. Sci.: Mater. Electron. **27**, 7899 (2016).
[70]A. Atarashi, M. Yagi, and S. Shirakata, Jpn. J. Appl. Phys. **53**, 05FW12 (2014).
[71]M. Akimoto, Q. Shen, S. Hayase, and T. Toyoda, Jpn. J. Appl. Phys. **53**, 07KB08 (2014).
[72]G. Cesarini, G. Leahu, M. L. Grilli, A. Sytchkova, C. Sibilia, and R. Li Voti, Phys. Status Solidi C **13**, 998 (2016).
[73]N. G. C. Astrath, F. Sato, F. Pedrochi, A. N. Medina, A. C. Bento, M. L. Baesso, C. Persson, and A. Ferreira da Silva, Appl. Phys. Lett. **89**, 231926 (2006).
[74]M. L. Gomez-Herrera, J. L. Herrera-Perez, P. Rodriguez-Fragoso, I. Riech, and J. G. Mendoza-Alvarez, Appl. Surf. Sci. **255**, 761 (2008).
[75]O. Vigil-Galán, J. R. González-Castillo, M. Macias, A. Cruz-Orea, F. A. Pulgarín-Agudelo, and E. Rodríguez, Phys. Status Solidi A **216**, 1900260 (2019).
[76]E. E. van Dyk and E. L. Meyer, Renew. Energy **29**, 333 (2004).
[77]D. Cahen, Rev. Sci. Instrum. **52**, 1306 (1981).
[78]B. Büchner, M. Wolf, and D. Cahen, Mater. Sci. Eng. A **122**, 127 (1989).
[79]B. Büchner, H. Flaisher, M. Wolf, and D. Cahen, J. Appl. Phys. **67**, 4338 (1990).
[80]A. C. Pereira, M. Zerbetto, G. C. Silva, H. Vargas, W. J. da. Silva, G. de. O. Neto, N. Cella, and L. C. M. Miranda, Meas. Sci. Technol. **3**, 931 (1992).
[81]A. Mandelis, *Diffusion-Wave Fields* (Springer, New York, 2001).
[82]P.-E. Nordal and S. O. Kanstad, Infrared Phys. **25**, 295 (1985).
[83]L. Eaves, H. Vargas, and P. J. Williams, Appl. Phys. Lett. **38**, 768 (1981).
[84]A. Mandelis, *Photoacoustic and Thermal Wave Phenomena in Semiconductors* (North-Holland, New York, 1987).
[85]O. Zelaya-Angel, J. J. Alvarado-Gil, R. Lozada-Morales, H. Vargas, and A. Ferreira da Silva, Appl. Phys. Lett. **64**, 291 (1994).
[86]T. Kawahara, Y. Ohbuchi, J. Morimoto, H. Goto, and T. Ido, Mater. Lett. **50**, 347 (2001).
[87]A. Pinto Neto, H. Vargas, N. F. Leite, and L. C. M. Miranda, Phys. Rev. B **41**, 9971 (1990).
[88]H. Yamamoto, I. Suemune, and M. Yamanishi, J. Appl. Phys. **60**, 2621 (1986).
[89]A. E. Sotnikov, M. A. Chernikov, and O. A. Ryabushkin, Instrum. Exp. Tech. **47**, 656 (2004).
[90]L. P. Avakyants, P. Yu. Bokov, I. P. Kazakov, M. A. Bazalevsky, P. M. Deev, and A. V. Chervyakov, Semiconductors **52**, 849 (2018).
[91]H. Masuda, A. Fujishima, and K. Honda, Bull. Chem. Soc. Jpn. **53**, 1542 (1980).
[92]H. Masuda, A. Fujishima, and K. Honda, Bull. Chem. Soc. Jpn. **55**, 672 (1982).
[93]Y. Maeda, A. Fujishima, and K. Honda, Bull. Chem. Soc. Jpn. **55**, 3373 (1982).
[94]R. E. Wagner and A. Mandelis, Phys. Rev. B **38**, 9920 (1988).
[95]R. E. Wagner and A. Mandelis, Appl. Spectrosc. **43**, 209 (1989).
[96]A. Mandelis, Anal. Sci. **6**, 491 (1990).
[97]J. Xia and A. Mandelis, Eur. Phys. J.: Spec. Top. **153**, 283 (2008).
[98]A. Mandelis and J. Xia, J. Appl. Phys. **103**, 043704 (2008).
[99]J. Xia and A. Mandelis, J. Appl. Phys. **105**, 062119 (2009).
[100]A. Melnikov, A. Mandelis, J. Tolev, and E. Lioudakis, J. Phys. Conf. Ser. **214**, 012111 (2010).

[101]J. Y. Liu, A. Melnikov, and A. Mandelis, Int. J. Thermophys. **36**, 987 (2015).
[102]Y. Zhang, A. Melnikov, A. Mandelis, B. Halliop, N. P. Kherani, and R. Zhu, Rev. Sci. Instrum. **86**, 033901 (2015).
[103]L. Hu, M. Liu, A. Mandelis, Q. Sun, A. Melnikov, and E. H. Sargent, Sol. Energy Mater. Sol. Cells **174**, 405 (2018).
[104]P. Song, F. Yang, J. Liu, and A. Mandelis, J. Appl. Phys. **128**, 180903 (2020).
[105]A. Melnikov, A. Mandelis, A. Soral, C. Zavala-Lugo, and M. Pawlak, ACS Appl. Electron. Mater. **3**, 2551 (2021).
[106]L. Hu, Z. Yang, A. Mandelis, A. Melnikov, X. Lan, G. Walters, S. Hoogland, and E. H. Sargent, J. Phys. Chem. C **120**, 14416 (2016).
[107]L. Hu, M. Liu, A. Mandelis, A. Melnikov, and E. H. Sargent, Prog. Photovolt.: Res. Appl. **25**, 1034 (2017).
[108]L. Hu, A. Mandelis, and Q. Sun, IEEE J. Photovolt. **9**, 132 (2019).
[109]K.-F. Berggren and B. E. Sernelius, Phys. Rev. B **24**, 1971 (1981).
[110]W. P. Dumke, Appl. Phys. Lett. **42**, 196 (1983).
[111]K. E. Newman, A. Lastras-Martinez, B. Kramer, S. A. Barnett, M. A. Ray, J. D. Dow, J. E. Greene, and P. M. Raccah, Phys. Rev. Lett. **50**, 1466 (1983).
[112]A. Nayak, G. L. Bhalla, and G. C. Trigunayat, Mater. Res. Bull. **35**, 2263 (2000).
[113]D. L. Wood and J. Tauc, Phys. Rev. B **5**, 3144 (1972).
[114]L. R. de Freitas, E. C. da Silva, A. M. Mansanares, G. Tessier, and D. Fournier, J. Appl. Phys. **98**, 063508 (2005).
[115]E. Sehn, K. C. Silva, V. S. Retuci, A. N. Medina, A. C. Bento, M. L. Baesso, A. Storck, and J. L. Gesztesi, Rev. Sci. Instrum. **74**, 758 (2003).
[116]R. Ahuja, H. Arwin, A. Ferreira da Silva, C. Persson, J. M. Osorio-Guillén, J. Souza de Almeida, C. Moyses Araujo, E. Veje, N. Veissid, C. Y. An, I. Pepe, and B. Johansson, J. Appl. Phys. **92**, 7219 (2002).
[117]E. L. Savi, R. F. Muniz, A. A. J. Silva, G. J. Schiavon, J. W. Berrar, F. R. Estrada, P. Schio, J. C. Cezar, J. H. Rohling, V. S. Zanuto, A. C. Bento, A. N. Medina, L. A. O. Nunes, and M. L. Baesso, J. Appl. Phys. **131**, 055304 (2022).
[118]M. Born and E. Wolf, *Principles of Optics Electromagnetic Theory of Propagation, Interference and Diffraction of Light*, 7th ed. (Cambridge University Press, 1999).
[119]J. A. Sampaio, T. Catunda, A. A. Coelho, S. Gama, A. C. Bento, L. C. M. Miranda, and M. L. Baesso, J. Non-Cryst. Solids **273**, 239 (2000).
[120]K. C. Silva, O. A. Sakai, A. Steimacher, F. Pedrochi, M. L. Baesso, A. C. Bento, A. N. Medina, S. M. Lima, R. C. Oliveira, J. C. S. Moraes, K. Yukimitu, E. B. Araújo, M. Petrovich, and D. W. Hewak, J. Appl. Phys. **102**, 073507 (2007).
[121]E. Pelletier, Handb. Opt. Constants Solids **2**, 57–73 (1998).
[122]C. Hu and J. R. Whinnery, Appl. Opt. **12**, 72 (1973).
[123]M. E. Long, R. L. Swofford, and A. C. Albrecht, Science **191**, 183 (1976).
[124]T. Higashi, T. Iamasaka, and N. Ishibashi, Anal. Chem. **55**, 1907 (1983).
[125]A. Marcano, H. Cabrera, M. Guerra, R. A. Cruz, C. Jacinto, and T. Catunda, J. Opt. Soc. Am. B **23**, 1408 (2006).
[126]J. Shen, R. D. Lowe, and R. D. Snook, Chem. Phys. **165**, 385 (1992).
[127]E. Dy, C. Gu, J. Shen, W. Qu, Z. Xie, X. Wang, M. L. Baesso, and N. G. C. Astrath, J. Appl. Phys. **131**, 063102 (2022).
[128]S. M. Lima, A. A. Andrade, R. Lebullenger, A. C. Hernandes, T. Catunda, and M. L. Baesso, Appl. Phys. Lett. **78**, 3220 (2001).
[129]M. L. Baesso, J. Shen, and R. D. Snook, J. Appl. Phys. **75**, 3732 (1994).
[130]O. S. Aréstegui, P. Y. N. Poma, L. S. Herculano, G. V. B. Lukasievicz, F. B. Guimarães, L. C. Malacarne, M. L. Baesso, S. E. Bialkowski, and N. G. C. Astrath, Appl. Spectrosc. **68**, 777 (2014).
[131]N. G. C. Astrath, L. C. Malacarne, M. L. Baesso, G. V. B. Lukasievicz, and S. E. Bialkowski, Nat. Commun. **5**, 4363 (2014).
[132]R. A. Cruz, M. C. Filadelpho, M. P. P. Castro, A. A. Andrade, C. M. M. Souza, and T. Catunda, Talanta **85**, 850 (2011).
[133]R. Silva, M. A. C. de Araújo, P. Jali, S. G. C. Moreira, P. Alcantara, and P. C. de Oliveira, AIP Adv. **1**, 022154 (2011).
[134]J. F. M. dos Santos, V. S. Zanuto, M. Ventura, C. B. Bramorski, T. Catunda, D. S. Manoel, L. C. Malacarne, and F. S. de Vicente, Phys. Rev. Mater. **3**, 115201 (2019).
[135]L. C. Malacarne, N. G. C. Astrath, P. R. B. Pedreira, R. S. Mendes, M. L. Baesso, P. R. Joshi, and S. E. Bialkowski, J. Appl. Phys. **107**, 053104 (2010).
[136]L. C. Malacarne, N. G. C. Astrath, G. V. B. Lukasievicz, E. K. Lenzi, M. L. Baesso, and S. E. Bialkowski, Appl. Spectrosc. **65**, 99 (2011).
[137]G. V. B. Lukasievicz, L. S. Herculano, E. Sehn, M. P. Belançon, S. E. Bialkowski, O. A. Capeloto, N. G. C. Astrath, and L. C. Malacarne, Appl. Spectrosc. **74**, 1274 (2020).
[138]T. P. Rodrigues, V. S. Zanuto, R. A. Cruz, T. Catunda, M. L. Baesso, N. G. C. Astrath, and L. C. Malacarne, Opt. Lett. **39**, 4013 (2014).
[139]L. C. Malacarne, N. G. C. Astrath, and L. S. Herculano, J. Opt. Soc. Am. B **29**, 3355 (2012).
[140]I. A. A. Terra, L. J. Borrero-Gonzalez, L. A. O. Nunes, M. P. Belancon, J. H. Rohling, M. L. Baesso, and O. L. Malta, J. Appl. Phys. **110**(8), 083108.
[141]A. K. Rufino Souza, A. P. Langaro, J. R. Silva, F. B. Costa, K. Yukimitu, J. C. Silos Moraes, L. Antonio de Oliveira Nunes, L. Humberto da Cunha Andrade, and S. M. Lima, J. Alloys Compd. **781**, 1119 (2019).
[142]F. B. Costa, K. Yukimitu, L. A. de O. Nunes, M. da. S. Figueiredo, J. R. Silva, L. H. da. C. Andrade, S. M. Lima, and J. C. S. Moraes, J. Am. Ceram. Soc. **100**, 1956 (2017).
[143]Z. Liu, J. Li, L. Yang, Q. Chen, Y. Chu, and N. Dai, Sol. Energy Mater. Sol. Cells **122**, 46 (2014).
[144]Y. Tai, G. Zheng, H. Wang, and J. Bai, J. Solid State Chem. **226**, 250 (2015).
[145]S. Ye, J. Zhou, S. Wang, R. Hu, D. Wang, and J. Qiu, Opt. Express **21**, 4167 (2013).
[146]P.-K. Kuo and M. Munidasa, Appl. Opt. **29**, 5326 (1990).
[147]J. W. Fang and S. Y. Zhang, Appl. Phys. B: Lasers Opt. **67**, 633 (1998).
[148]B. Li, H. Blaschke, and D. Ristau, Appl. Opt. **45**, 5827 (2006).
[149]N. G. C. Astrath, L. C. Malacarne, P. R. B. Pedreira, A. C. Bento, M. L. Baesso, and J. Shen, Appl. Phys. Lett. **91**, 191908 (2007).
[150]G. V. B. Lukasievicz, N. G. C. Astrath, L. C. Malacarne, L. S. Herculano, V. S. Zanuto, M. L. Baesso, and S. E. Bialkowski, Appl. Spectrosc. **67**, 1111 (2013).
[151]F. Sato, L. C. Malacarne, P. R. B. Pedreira, M. P. Belancon, R. S. Mendes, M. L. Baesso, N. G. C. Astrath, and J. Shen, J. Appl. Phys. **104**, 053520 (2008).
[152]T. G. M. Bonadio, R. R. Pezarini, A. N. Medina, V. S. Zanuto, M. L. Baesso, D. Z. Montanher, L. S. Herculano, C. Jacinto, and N. G. C. Astrath, Phys. B **605**, 412713 (2021).
[153]V. S. Zanuto, L. S. Herculano, M. L. Baesso, G. V. B. Lukasievicz, C. Jacinto, L. C. Malacarne, and N. G. C. Astrath, Opt. Mater. **35**, 1129 (2013).
[154]O. A. Capeloto, G. V. B. Lukasievicz, V. S. Zanuto, L. S. Herculano, N. E. Souza Filho, A. Novatski, L. C. Malacarne, S. E. Bialkowski, M. L. Baesso, and N. G. C. Astrath, Appl. Opt. **53**, 7985 (2014).
[155]N. G. C. Astrath, F. B. G. Astrath, J. Shen, J. Zhou, C. E. Gu, L. C. Malacarne, P. R. B. Pedreira, A. C. Bento, and M. L. Baesso, Appl. Phys. B **94**, 473 (2009).
[156]N. G. C. Astrath, L. C. Malacarne, V. S. Zanuto, M. P. Belancon, R. S. Mendes, M. L. Baesso, and C. Jacinto, J. Opt. Soc. Am. B **28**, 1735 (2011).
[157]O. A. Capeloto, V. S. Zanuto, G. V. B. Lukasievicz, L. C. Malacarne, S. E. Bialkowski, T. Požar, and N. G. C. Astrath, Appl. Phys. Lett. **109**, 191908 (2016).
[158]P. P. González-Borrero, G. V. B. Lukasievicz, V. S. Zanuto, N. G. C. Astrath, and L. C. Malacarne, J. Appl. Phys. **121**, 195101 (2017).
[159]T. V. Moreno, V. S. Zanuto, N. G. C. Astrath, G. R. Silva, E. J. S. Fonseca, S. T. Souza, D. Zhao, H. Jain, and L. C. Malacarne, Opt. Mater. **94**, 9 (2019).
[160]W. Nowacki, *Thermoelasticity* (Elsevier, 1986).
[161]G. S. Bianchi, V. S. Zanuto, F. B. G. Astrath, L. C. Malacarne, I. A. A. Terra, T. Catunda, L. A. O. Nunes, C. Jacinto, L. H. C. Andrade, S. M. Lima, M. L. Baesso, and N. G. C. Astrath, Opt. Lett. **38**, 4667 (2013).
[162]S. T. Souza, E. J. S. Fonseca, C. Jacinto, N. G. C. Astrath, T. P. Rodrigues, and L. C. Malacarne, Opt. Mater. **48**, 71 (2015).